

**Insights into the Mechanics of En-Échelon Sigmoidal Vein
Formation using Ultra-High Resolution Photogrammetry
and Computed Tomography**

Samuel T Thiele^{a*}
Steven Micklethwaite^a, Paul Bourke^b, Michael Verrall^c, Peter Kovesi^a

^aCET (M006), School of Earth and Environment, The University of Western Australia, 35 Stirling Highway, Crawley, WA 6009. Australia.

^bIVEC (M024), Faculty of Engineering, Computing and Mathematics, The University of Western Australia, 35 Stirling Highway, Crawley, WA 6009. Australia

^cAustralian Resources Research Centre (ARRC), 26 Dick Perry Avenue, Kensington WA 6151, Australia

Keywords: Sigmoidal Veins, Pressure Solution, Photogrammetry, Computed Tomography

ABSTRACT

Two novel techniques, photo based reconstruction (photogrammetry) and computed tomography (CT), are used to investigate the formation of an exceptional array of sigmoidal veins in a hand sample from Cape Liptrap, Southern Victoria, and to provide constraint on models for their development. The accuracies of the photogrammetric models were tested by comparison with a laser scan generated three dimensional (3D) model. The photogrammetric model was found to be accurate to at least 0.25mm and substantially more detailed than the laser scan. A methodology was developed by which 3D structural measurements could be extracted from the photogrammetric model. This was augmented with the CT model which, through its capacity to elucidate internal structure, was used to constrain the geometry and linkage of structures within the rock volume. The photogrammetric and CT data were then combined with detailed photomicrographs to evaluate the evolution of the sigmoidal veins in the sample.

The angle between the sigmoidal vein margins and an inferred shear zone, as well as the orientations of the crystal fibres, were found to imply a rotation of $>27^\circ$. However coeval pressure solution seams and older veinlets in the rock bridges between the veins were only found to have rotated by $\sim 10^\circ$, an observation not easily explained using existing models for sigmoidal vein formation.

A new model is proposed in which a significant component of sigmoidal vein geometry is due to localised dilation caused by slip on the pressure solution seams. The process involves strain partitioning onto pressure solution seams, which leads to exaggeration of sigmoidal vein geometries. If not accounted for, the apparent vein rotation due to slip partitioning introduces errors into calculations of simple shear and volume strain based on sigmoidal arrays of this type. Furthermore, the CT data demonstrated that in 3D the veins are continuous and channel-like, implying a far higher degree of connectivity and fluid transport than is suggested by their 2D form.

1. Introduction

The development of faults and shear zones is a common response to local and far-field stress. Fracturing, fluid flow and vein formation accompanying these processes are critical for the formation of mineral deposits (Micklethwaite et al., 2010), and present day manifestations of these processes provide important information for interpreting the paleo-environments that have shaped these systems.

Sigmoidal veins are a class of en-échelon vein characterised by their unusual S or Z shaped geometry, and are common within deformed sedimentary rocks (Beach, 1975). There has been considerable uncertainty over the mechanisms controlling the formation of sigmoidal veins (Beach, 1975; Nicholson and Pollard, 1985; Rickard and Rixon, 1983; Tanner, 1992), and hence how best to interpret their significance in terms of far-field palaeostress orientations, principal strain axes and strain evolution over time (eg. Belayneh and Cosgrove, 2010; Lisle, 2013). Despite this uncertainty, a simplistic model involving progressive rotation of extension veins forming within a shear zone (Beach, 1975) has become established, and is largely accepted uncritically (eg. Davis et al., 1996; Fossen, 2010; Twiss and Moores, 2007).

This study achieves two objectives. Primarily we examine the formation of sigmoidal veins using a rock sample collected from Cape Liptrap, Victoria, which contains a well-preserved sigmoidal vein array. Secondly we demonstrate application of novel high-resolution photogrammetric and tomographic methods to structural geology, examine accuracies of the photogrammetric models and develop techniques for extraction of structural orientation data. Photogrammetry and computed tomography (CT) techniques are non-destructive imaging techniques that allow detailed structural information to be extracted in three dimensions (3D). In this study, these techniques were applied to the Cape Liptrap sample and a workflow developed by which uncertainties in the resulting models could be assessed and 3D structure maps produced, without damaging the integrity of the

specimen. The 3D structure maps were used to interpret the formation of the vein array, including an assessment of the sample in the context of published models for sigmoidal vein formation.

1.1 – Geological Setting

The study sample was collected from the Early Devonian Liptrap Formation, exposed at Cape Liptrap in southern Victoria (Fig. 1a). The Liptrap Formation is a turbidite sequence, comprising competent carbonate-rich sandstone layers separated by incompetent, laterally continuous shale layers (Douglas, 1972; Gray et al., 1999). The formation has been metamorphosed to lower greenschist facies, and is tightly folded and cut by small-displacement reverse faults associated with the middle Devonian Tabberabberan orogeny (Gray et al., 1999; Lennox and Golding, 1989). Gray et al. (1999) used microstructural and fluid inclusion data to suggest that folding of the Liptrap formation occurred at a depth of ~6–8km and temperatures of 200–400°C.

The study sample is approximately 45cm long, 20cm wide and 15cm deep and is comprised of homogeneous carbonate-rich sandstone with an isotropic, equigranular fabric (Fig. 1b). The veins contained in the sample are filled with fibrous and blocky calcite. They occur at a range of scales, and are here classified into three different categories, based on their thickness: veins less than ~1mm thick are classified as veinlets, veins with thicknesses of ~1–5mm as minor veins and veins with a thickness >5mm as major veins. Only the major veins have developed sigmoidal geometries. These are accompanied by widespread narrow pressure solution seams up to ~6 cm in length.

The composition of the sample suggests that it is derived from one of the carbonate-rich sandstone layers in the Liptrap Formation, and it is reasonable to infer that it is related to the small reverse faults developed in the folds, which are associated with localised vein formation. Because the sample was not *in situ* when collected, the original orientations of the veins are unknown.

(Figure 1 here)

1.2 – Models of Sigmoidal Vein Formation:

Fractures forming under extension (Mode I) and shear (Mode II) are expected to form roughly elliptical, planar structures in a homogeneous rock mass. As such, sigmoidal veins require special explanation.

Several models have been proposed for the formation of sigmoidal vein arrays (Fig. 2). Beach (1975), drawing on prior work by Shainin (1950) and Riedel (1929), proposed a kinematic model in which Mode I fractures developing within an existing shear zone become progressively rotated by simple shear, while their tips continue to propagate parallel with the maximum compressive stress axis, and hence develop a sigmoidal geometry (Fig. 2a).

Nicholson and Pollard (1985) presented an alternative mechanical model to demonstrate that the mechanical strength of the rock bridges between adjacent veins can control vein dilation. As a result, when planar, en-échelon fracture arrays form and grow the rock bridges between them can deform as independent beams, progressively buckling under further stress and creating sigmoidal vein dilation (Fig. 2b). In contrast to the previous model, this model suggests that shear offset across the tabular zone occupied by sigmoidal veins results from the vein growth and rock bridge mechanics, rather than the veins developing in a pre-existing shear zone.

Finally, Pollard et al. (1982) and Olson and Pollard (1991) used Linear Elastic Fracture Mechanics (LEFM) to demonstrate that closely spaced propagating vein tips will interact with each other. Olson and Pollard (1991) showed that this interaction alone can cause sigmoidal fracture geometries (Fig. 2c), while Pollard et al. (1982) provide a mechanism for generating en-échelon vein arrays outside of a shear zone, suggesting that they can form on the margins of a 'parent fracture' due to small spatial or temporal changes in local stress fields.

The different models for sigmoidal vein formation can be distinguished by predictions they make regarding vein geometry, fibre orientations and deformation of the rocks surrounding the veins (Table 1). These predictions were tested against the structures observed in the Cape Liptrap sample.

(Table 1 & Figure 2 here)

118

119 **Methods**

120 Photogrammetry is a method by which photographs of an object, captured from two or more
121 positions, are used to extract 3D information. Stereophotography, used extensively and for many
122 years by cartographers and geologists, is a form of photogrammetry (Bemis et al., 2014).

123 Recent improvements in digital photography and the development of a computational technique
124 called Structure from Motion (SfM, Sturm and Triggs (1996)) has allowed the generation of fully 3D
125 models from spatially unconstrained imagery (Bemis et al., 2014). This technique gives geoscientists
126 a much needed method to objectively and quantitatively capture 3D form and texture in exquisite
127 detail.

128 SfM algorithms identify common points between image pairs in a set (Lowe, 2004), calculate lens
129 parameters such as focal length (Pollefeys et al., 1999), and then calculate the relative 3D location
130 and orientation of each camera and matched feature using an optimization process known as
131 'bundle adjustment' (Triggs et al., 2000). This produces a 3D point cloud from which a textured
132 mesh can be built using triangulation techniques (Fabio, 2003) and projection of the original images
133 onto its surface. Illustrated details of the method and its application to structural geology are
134 presented in Bemis et al., (2014).

135 However for this data to be useful it is necessary to first assess the accuracy and resolution of the
136 photogrammetric model. For this reason, several independent photogrammetric datasets
137 representing the 3D form and structure of the Cape Liptrap sample were compared with each other
138 and with a reference dataset derived by laser scanning. A computerised tomography (CT) scan was
139 also generated to help constrain the geometry of structures within the rock volume.

2.1 – Data Collection

2.1.1 – Sample preparation

Accurate scaling of photogrammetric models requires spatial reference points with known locations (Bemis et al., 2014; Favalli et al., 2012). These reference points also help avoid distortions during photogrammetric processing. For this study, 25 reference points evenly distributed over the sample surface were used to spatially reference the photogrammetric models. Distances between each reference point were measured using a pair of electronic callipers accurate to ± 0.01 mm. A plastic scale plate with small metal bolts glued to it was also attached to the rock, to allow alignment of the CT-scan (see below) with the photogrammetric models.

2.1.2 – Photography

Four different sets of photographs of the sample were taken in order to trial different photographic techniques and ensure a highly accurate model was produced. Photoset 1 was captured using a Canon EOS 5D Mark III DSLR camera with a 100mm fixed focal length lens, and comprised photographs taken in strips 10° apart as the sample was rotated about both its long axis and an orthogonal axis on a rotating stage fitted with a 10° ratchet. Diffuse lighting was employed to avoid shadows. The camera was mounted on a tripod so that suitable exposure times (~ 1 second) could be used and to avoid motion blur. The extremities of the sample were captured using an unmounted camera. Each image frame covered a surface area of approximately 8×10 cm with a $\sim 1/3$ overlap with adjacent images. A total of 516 photographs were captured, concentrated around the vein set (as this is the area of interest in the sample).

Since the sample has a complex 3D morphology it was not possible to fully focus some portions of the images. To minimize this problem, photographs were captured using small apertures (F-stop 17) to maximise depth of field.

Photosets 2–4 were captured by mounting the sample on a stationary clamp and photographing it from different locations, maintaining $\sim 30\%$ overlap between images. Photosets 2–3 were generated

using the Canon EOS while Photoset 4 was captured using a Canon PowerShot S95 simple compact digital camera. In all three cases, because the camera and tripod had to be moved between each image, the number of photographs that could be taken was limited due to time constraints, hence limiting the amount of detail that could be resolved from the photoset. Photosets 2, 3 and 4 contained 307, 52 and 87 photographs respectively.

2.1.3 – Laser Scanning

3D laser scanning, a technique whereby a laser beam is used to accurately measure the location of a grid of points on the surface of an object, was performed at 2000 dpi using a NextEngine 2020I HD™ laser scanner, which has a reported accuracy of 0.127 mm (Slizewski and Semal, 2009). A total of 15 scans were done, each from different angles.

2.1.4 – Microscopy

A series of high resolution photomicrographs were captured of the veins in order to properly resolve cross-cutting relationships between the different vein generations and pressure solution seams. These were captured using an arm-mounted Leica 6D stereo-microscope fitted with a Nikon DS-Fi2 camera. Focus stacking, a technique for enhancing depth of field by combining multiple images (Piper, 2010), was used in many of the photographs to avoid significant focal blur caused by the limited depth of field of the microscope.

A photogrammetric model, generated from a grid of photomicrographs of selected veins was also created (see section 3.2.1). In order to avoid systematic artefacts such as subtle concave distortions (James and Robson, 2014), the photomicrograph grids were captured with the camera in both landscape and portrait orientations (Bemis et al., 2014).

2.1.5 – CT Scanning

The sample was scanned using a Siemens SOMATOM Definition AS 64-slice medical CT scanner, in 1275 slices using an X-ray beam generated at 120kV and 500mA. The volumetric resolution of the resulting model was 512×512×1275 voxels, each 0.5 mm³. Due to high noise levels in the dataset the

CT scan was subsampled by a factor of two, producing a final smoothed tomographic model with 1 mm³ resolution.

2.2 – Data Processing

2.2.1 – Photogrammetry

Photogrammetric models were constructed using the commercial software package Agisoft Photoscan™. Processing time was reduced by running the software on a PC with 256 GB of RAM, 48 Intel Xeon E5-2697 (2.7GHz) processors, and NVIDIA Quadro K5000 and Tesla K20c graphics cards.

After loading images, all out-of-focus and background regions were manually masked out to improve point matching accuracy. Photographs were then aligned in 3D space, and a sparse point cloud generated. Models containing reference points were spatially referenced by manually locating the points in the images and constraining distances between them using the measured values.

The sparse point cloud was then densified to produce a significantly higher resolution dense point cloud, which was used to construct a triangulated mesh representing the estimated geometry of the sample's surface. Meshes with large numbers of elements were simplified by decimation to contain 1 million triangles, so that they could be rendered and manipulated on an ordinary PC.

“Texture mapping” improves the information represented by triangulated meshes by projecting the original 2D photographs onto the 3D mesh surface, to produce a surface containing detail and colour not captured by the geometry alone. Because texture quality is sensitive to poor-quality and unfocused images, low-quality photographs were removed from the dataset and extended masks used to remove unfocused portions of the photographs before generating the textures.

A photogrammetric model was constructed in this way from each of the four Photosets. Model A was derived from Photoset 1 (516 images). Initial camera alignment produced a sparse point cloud of 1,497,646 points in ~5hrs of processing. The dense point cloud comprised 210,118,817 points generated in ~11hrs. The dense point cloud was used to generate two meshes, one of the whole

sample and one of the area of interest (the vein set) only. Both meshes were decimated to 1 million triangles.

Models B and C were derived from Photosets 2 and 3 respectively. Model B was derived from 307 photographs with the mesh decimated to 1 million triangles as in Model A. Model C was derived from 52 photographs, but only captured the region of the sample containing the sigmoidal vein set.

Model D was derived from the 87 photographs in Photoset 4. This model had 98,803 vertices and 197,215 triangles.

Finally, the grid of 45 photomicrographs was used to produce a model comprising 2,325,997 points. The textured mesh produced from this point cloud contained 466,970 faces and 234,381 vertices.

2.2.2 – Comparison Maps

Laser scans were aligned using ScanStudioHD Pro™ and then merged using ArtecStudio9™ to produce a complete model of the rock with 376,875 vertices and 753,746 faces. Photogrammetric models were compared to the laser scan model using a method similar to that of Favalli et al. (2012). The composite laser scan was aligned with each of the photogrammetric models, using the Align tool in Meshlab (Cignoni et al., 2008) and differences calculated using the open source tool Metro (Cignoni et al., 1998).

Metro writes the distance between the two meshes being compared to each vertex, allowing the creation of difference maps. Conveniently, Meshlab has a 'Mesh Quality' tool that was used to map different colour ramps to these vertex values and produce coloured difference maps.

Histograms describing the area of each mesh with nominated error values were also generated, and used to calculate mean absolute error (MAE) and a scale invariant percentage error (%Err) derived by dividing the MAE by the average linear dimensions of the model. Root mean square error (RMSE) was not used to compare the models (c.f. Favalli et al., 2012) because RMSE varies with both

average error magnitude and error variance, giving too much weighting to higher error values (Willmott and Matsuura, 2005).

2.2.3 – CT segmentation

The open-source software package Dristhi (Limaye, 2012), developed for manipulating and rendering 3D tomographic datasets, was used to segment the CT scan into veins, pressure solution seams and background. Due to the low density contrast between the host rock and calcite vein filling, segmentation could not be performed automatically. Instead, each horizontal slice within the tomographic model was manually interpreted and voxels classified as host rock, vein fill or containing substantial pressure solution. This method of segmentation was sufficient to determine the general form of the structures in 3D space.

2.3 – Structure Mapping

A 3D map interpretation of the sigmoidal vein set and associated veinlets, pressure solution seams and crystal fibres was created using the most accurate photogrammetric model (Model A). Because of the 3D nature of the sample, two dimensional (2D) GIS software such as ArcGIS was not appropriate to perform the mapping. Instead, the open source 3D-graphics package Blender (www.blender.org) was used.

Structures were digitised in Blender using the Grease Pencil tool to project lines onto the surface of the photogrammetric model, producing a 3D representation of structures exposed on the surface of the sample. A Python script (provided in the Supplementary Materials) was written to export these features to CSV format so they could be interpreted in other software such as ArcGIS™ or OpenStereo (Grohmann and Campanha, 2010).

2.4 – Extraction of Planes

Because the surface of the Cape Liptrap sample is not planar, it is possible to extract 3D orientations from selected points along structures mapped onto its surface, relative to an arbitrary coordinate system; akin to the classic ‘three-point problem’. A Java application was developed (provided in the

Supplementary Materials) that estimates a plane of best fit for features in the structure maps using an implementation of the Random Sample And Consensus (RANSAC) algorithm (Fischler and Bolles, 1981).

The Java application takes CSV files containing sets of edges (defined by two vertices) and builds them into multi-segment lines based on shared vertices (Fig. 3a). Each line is then divided into samples (Fig. 2b) of 500 vertices (or less at the tips), a length of ~5mm. For each of these samples the second and third largest principal components (C_2 and C_3) are calculated and used to assess the planarity (P) of the data using:

$$P = 1 - \frac{C_3}{C_2} \quad (1)$$

Samples that perfectly define a plane have planarity=1 (as $C_3=0$), while samples representing either a line or random point cloud have planarity=0 as C_2 and C_3 either approach zero or are equal. If planarity is deemed to be sufficient ($P > 0.75$) the sample is processed using the RANSAC algorithm to produce a plane of best fit (Fig. 3c–e).

In this context, the RANSAC algorithm functions by iteratively calculating the number of points (inliers) that fit within a threshold distance (0.1 mm) of a plane defined by three randomly selected points. Random planes are tested until the number of trials (N) exceeds that required to be statistically confident the ‘correct’ plane has been tried at least once (Eq. 2), given the greatest number of inliers so far achieved (i) and total dataset size (n). The model with the greatest number of inliers is then returned as the estimate of the plane of best fit.

$$N \geq \frac{\log(1-0.99)}{\log\left(1-\frac{i}{n}\right)} \quad (2)$$

Finally, in order to remove some of the random variation introduced by using a stochastic estimation technique, the model is further refined by performing least squares regression on the samples deemed to be inliers by the RANSAC algorithm (Fig. 3f). Because many of the surfaces of the

sample (and hence also the photogrammetric model) are flat, and some of the veins are not perfectly planar, this method generates a few false orientations, sub-parallel with the surface of the sample. These data were not removed however, as they are relatively few in number and they do not significantly influence the statistics.

(Figure 3 here)

2.5 – Measurement of wall-fibre angles

Angles between vein walls and the calcite fibres were measured manually using the 3D model and a protractor-like tool in Blender. Angles were all measured clockwise from the vein wall to the fibre, so that the wall-fibre angle is consistent on either side of the vein. A Python script was used to export the angles and their locations to a CSV file for analysis.

3. Results

3.1 – Photogrammetric Model Accuracy

Comparisons between photogrammetric models and the laser scan model (Fig. 4) showed that Model A (Fig. 4–7) was the most accurate, with MAE=0.59 mm and percent error of 0.22%. It is worth noting that much of this 0.22% error is derived from the two ends of the sample, which were not a focus of this study and hence photographed in less detail. The corners of each model generally have the lowest accuracies (Fig. 4). Likewise, small errors in the orientation of planar faces appear to cause gradual increases in error, such as is observed on the front face of Model C (Fig. 4). Errors are all less than 0.5%, which is equivalent to the results reported by Favalli et al. (2012).

Mapping the x, y and z components of the normal of each mesh element to red, green and blue colour values enables visual representation of the geometric detail of each model (Fig. 4 and 5). The geometric detail captured by each model increases with the number of photographs. Topographic features such as weathered pressure solution seams are represented much more crisply in Model A;

indeed, the resolution of Model A is sufficient that some of the vein fibres are discernible in the normal map alone (Fig. 5).

The majority of the face containing the sigmoidal veins in Model A is accurate to within ~ 0.25 mm (Fig. 5). Apparent errors around the margins of the veins and within small pits on the model surface arise because the photogrammetric model resolves these features in much finer detail than the laser scan (Fig. 5). This observation suggests that Model A potentially has greater accuracy than the laser scan, although there is no quantitative method for verifying this at the present time.

(Figure 4 & 5 here)

The texture for Model A is also superior to the other models. Model B and C have somewhat blurry texture maps, while the lighting and contrast of the texture maps produced for Model D make it difficult to resolve features such as vein fibres. The texture map produced for Model D was also somewhat lower resolution (as were the images used to produce it).

3.2 – Structures

Veins, crystal fibres and pressure solution seams are clearly resolvable in the photogrammetric models (Fig. 6). These structures were mapped, and measurements of their orientations extracted at selected points along their surfaces, as well as their relationships with crystal fibres (Fig. 7). A reference frame was defined such that the top of the sample represented north (top of Fig. 7) and the surface containing the sigmoidal veins defined as horizontal. The orientations of major and minor veins were acquired along both sides of the veins (e.g. two lines per feature), while veinlets were measured along a single line. The surface traces of the crystal fibres and pressure solution seams were also mapped as lines, although the location of the pressure solution seams is often rather imprecise due to their irregular geometry and because they are preferentially eroded. Planar orientations for many of the veins and pressure solution seams were successfully extracted using the RANSAC method outlined above.

(Figure 6 here)

3.3 – Structure Orientations

3.3.1 – Vein and Pressure Solution Seam Orientation

Calculated vein and pressure solution seam orientations are plotted as poles in Fig. 7. The eigenvectors of these data were used to estimate population means (Allmendinger et al., 2011), which are presented in Table 2 and on the stereonets in Fig. 7.

Orientation data collected for the pressure solution seams contained considerable variation, due to their irregular structure and difficulties mapping their precise location. Notwithstanding this, the pressure solution seam poles form broad clusters around $20^{\circ} \rightarrow 300^{\circ}$, $7^{\circ} \rightarrow 094^{\circ}$. These orientation clusters correspond with trends evident in the structure map (Fig. 7). The mean orientation of the pressure solution seams is approximately perpendicular to the vein orientations. The 95% confidence intervals for the mean orientation of the major veins, minor veins and veinlets overlap, and hence they cannot be considered to have significantly different orientations. The average orientation of all the veins in the sample was $128.6^{\circ}/88.6^{\circ}\text{W} \pm 5.9^{\circ}$.

An envelope was defined around the vein array based on a systematic coincidence of vein tips, sudden changes in orientation, shear offsets and zones of increased dilation (Fig. 8a). This envelope is interpreted to represent the boundaries of a zone of incipient shear, and is divided into zones of maximum, intermediate and minor apparent rotation.

The intersection angles between calculated structure orientations and the interpreted shear zone have been calculated. Because structure orientations could only be extracted from areas with topographic relief this data has been complemented with angles measured in 2D. These angles were measured at 2mm intervals from the zone centre (Fig 8a). Because the main face of the sample approximates a profile section through the array, these angles approximate the true angle of intersection.

These structure-shear envelope angles, displayed as boxplots in Fig. 8b, suggest that structure orientations change systematically across the vein array. Average structure-envelope angles have been used to calculate the amount of apparent rotation that would be required to explain the changes in vein orientation across the shear envelope (Table 3). The orientations of both the non-sigmoidal veins (minor veins and veinlets) and pressure solution seams suggest that they have rotated by $\sim 10^\circ$ on the front face of the specimen toward the centre of the shear envelope. By contrast, the sigmoidal veins have substantially greater apparent rotations of $\sim 27^\circ$. Many portions of the sigmoidal veins have apparent rotations of $>45^\circ$ (Fig. 8).

3.3.2 – Vein Fibre Orientation

Individual crystal fibres within the sigmoidal veins can be tracked across the full width of the veins (Fig. 7 and 9), suggesting that the fibres are roughly oriented within the mapping plane (i.e. they do not plunge in and out of the surface of the sample). Hence the mapped orientation approximates the orientation of the long (c)-axis of the crystals themselves. These fibres generally trend perpendicular to the veins; however, there is substantial variation within the population. This variation appears to be spatially controlled (Fig. 9), with the mean orientation of vein fibres equal to 042° in vein tips and 070° within vein centres (a difference of $\sim 28^\circ$). Many individual fibres in the vein centres are oriented at $>40^\circ$ to fibres in the vein tips, trending close to 090° .

The angle between vein fibres and vein walls also varies spatially. Fibre-wall angles are generally equal to 90° , but there is a marked divergence from this relationship where the sigmoidal vein walls bend sharply (Fig. 9).

(Table 2 and Table 3 here)

(Figure 7, 8 and 9 here)

3.4 – *Overprinting Relationships*

Overprinting relationships were examined at millimetre scales using the photomicrographs and photogrammetric models constructed from them (included as Supplementary Material). These relationships were integrated with the macro-scale photogrammetric models to interpret the relative timing of structures observed in the sample.

Representative photomicrographs illustrate systematic crosscutting relationships observed between the various vein types and pressure solution seams (Fig. 10). Most pressure solution seams crosscut the veinlets and minor veins (Fig. 10b–g, i and j), whereas only a few were observed crosscutting the larger sigmoidal veins. The sigmoidal veins also crosscut veinlets and minor veins in several locations (Fig. 10a–f and j). Only one location was observed where a veinlet appears to crosscut one of the sigmoidal veins (Fig. 10h) but this observation is somewhat ambiguous.

Many of the overprinting relationships observed between the minor veins and pressure solution seams are mutually crosscutting, with minor veins often crosscut by several pressure solution seams, partially crosscut by some, and crosscutting others. The pressure solution seams often appear to separate zones that have undergone varying amounts of strain, or that have accommodated strain in different ways. For example, some domains develop many fractures with small dilations whereas others develop fewer fractures with larger dilations (eg. Fig. 10f and i, Fig. 11).

(Figure 10 here)

3.5 – *Vein Geometry*

Integration of the photogrammetric and CT models provides detailed constraints on the 3D geometry of the major veins and to a lesser extent the pressure solution seams within the sample. Blocky calcite vein filling is associated with increased x-ray attenuation while fibrous calcite filling results in decreased x-ray attenuation (Fig. 12a–c). Pressure solution seams are also expressed in the CT data, as faint but distinct bands of increased x-ray attenuation (Fig. 12a). Interpretation of these

structures allowed the construction of a 3D polygonal hull representing the vein set and some of the associated pressure solution seams (Fig. 12d).

The vein set exposed on the top surface of the sample (Fig. 6a and 7) is dominated by large, sigmoidal veins. The central sections of these veins are oriented obliquely to their tips, inclined in a clockwise direction. These veins also appear to have undergone substantially more dilation towards the centre of the shear zone hosting the array than at its margins (Fig. 7 and 8). A large number of pressure solution seams are present around the veins (Fig. 7), and are more intensely developed towards the centre of the shear zone. These pressure solution seams can extend beyond the bounding envelope of the vein array. In a few places, seams of different orientations link together and form polygonal networks.

The CT model suggests that about 4.5cm into the sample the pressure solution seams disappear and the vein set changes dramatically. One vein disappears altogether, while the two largest sigmoidal veins merge (Fig. 12a, c and d). Below this point the veins appear much more planar. Finally the vein geometry approaches the relatively planar, non-sigmoidal geometry observed on the bottom face of the sample (Fig. 6b, 12a and d). Significantly, the geometry of the veins in 3D resemble channel-like structures that are continuous beyond the dimensions of the sample.

The minor veins and veinlets in the sample are generally planar. The photomicrographs highlight complex interactions between these veins and the pressure solution seams on the front face of the sample. Many of the veins undergo large changes in dilation where they are crosscut by pressure solution seams (Fig. 11), and many veins also appear to be truncated by the pressure solution seams (Fig. 10i and 11d). Fig. 11 also shows that some of the pressure solution seams have developed shear offset. While these offsets are not always dextral (eg. Fig. 11a), the offsets are kinematically consistent with the overall shear zone. Offsets do not appear to have developed outside of the sigmoidal vein array.

The amount of offset across pressure solution seams appears to be controlled by orientation; offsets are only observed on seams that are not perpendicular ($>\pm 10^\circ$ difference) to the sigmoidal vein tips. These relationships are interpreted to arise from slip partitioning where shear strain resolves along the pressure solution seams but the microlithons between the pressure solution seams undergo extension parallel with the movement direction.

Offsets on the pressure solution seams also appear to affect the sigmoidal veins (Fig. 13). Sections of the sigmoidal veins with substantially different orientations correlate with intersecting pressure solution seams and changes in vein aperture.

(Figure 11, 12 and 13 here)

4. Discussion – Formation, Dilation and Linkage of Sigmoidal En-Échelon Veins

Structural mapping, photomicrographs and computed tomography have allowed an interpretation of the processes that led to the development of the observed vein array. These processes must explain the geometry of the sigmoidal veins on the top face of the Cape Liptrap sample, their transition and linkage to form essentially planar veins on the bottom face of the sample and the inconsistent distribution of pressure solution seams and veinlet damage in an otherwise apparently homogeneous rock mass. Furthermore these processes must explain the $\sim 10^\circ$ change in non-sigmoidal vein and pressure solution seam orientation across the array, in contrast to the adjacent $>27^\circ$ change in orientation of the central portion of the sigmoidal veins and the $>40^\circ$ range in calcite fibre orientations.

4.1 – Timing

Overprinting relationships allow the relative timing of the last increment of strain on each structure in the sample to be established (Fig. 14). The veinlets represent the earliest episodes of strain, as they are crosscut by all other structures (with a possible single exception), potentially accompanied

by coeval pressure solution. Progressive deformation led to the development of minor veins as strain increased. Dilation of these veins appears to have been accommodated by partitioning of slip along pressure solution seams, giving the appearance of extreme truncation (Fig. 10i and 11d). Finally, the large sigmoidal veins developed, crosscutting minor veins, veinlets and pressure solution seams in several locations (Fig. 10b–d, f, and j). In a few locations these sigmoidal veins are in turn crosscut by some of the major pressure solution seams, indicating that activity on some of the pressure solution seams continued to develop after vein formation had ceased.

This sequence of events suggests that strain in the array has progressively localised onto fewer, but larger, structures through time.

(Figure 14 here)

4.2 – Constraining Models of Sigmoidal Vein Formation

The structural data collected from the photogrammetric and CT models allow predictions of different models for sigmoidal vein formation (Table 1) to be tested.

Vein linkages observed in the CT model suggest that interactions between the veins have occurred, however this cannot explain the geometry of the sigmoidal veins as in the vein-tip interaction model of Olson and Pollard (1991). The vein tips of sigmoidal veins formed by this mechanism will be misoriented with respect to the far-field stress, not vein centres (Table 1). The similar orientation of the early formed veinlets, the major planar veins observed on the bottom face of the sample and the tips of the sigmoidal veins suggest that they were oriented parallel to the maximum far field stress orientation, and it is the sigmoidal vein centres that became misoriented. Furthermore, vein-tips of sigmoidal veins formed by a vein-tip interaction mechanism would be expected to crosscut older structures such as the veinlets. This was not observed.

Similarly, the sigmoidal vein geometries could also be attributed to a counter-clockwise rotation of the far-field principal stresses that occurred during the evolution of the vein array. However if this

were the case, the sigmoidal vein tips would not be sub-parallel to the older veinlets, as has been observed.

The model of Beach (1975) attributes the geometry of sigmoidal veins to progressive rotation of propagating veins during shearing, and requires that any older structures in the shear zone also be rotated (Table 1). The change in orientation of structures across the shear zone (Fig. 8) suggests that progressive rotation of this type may have occurred; however this rotation cannot have exceeded the $\sim 10^\circ$ rotation recorded by the older veinlets, minor veins and pressure solution seams (Table 3). The orientation of the central portions of the sigmoidal vein walls and $>40^\circ$ range in orientation of many of the crystal fibres observed in the central portion of some of the veins (Fig. 9) requires substantially more than a 10° rotation. This suggests that another process is exaggerating the geometry of the veins while not causing further rotation of older structures in the rock, and that while rotation may be partially responsible for the sigmoidal vein geometries observed in the sample, it cannot fully explain them.

The $\sim 10^\circ$ rotation of the veins and pressure solution seams could also be attributed to buckling of rock bridges separating the veins, in accordance with the model of Nicholson and Pollard (1985). The generally consistent thickness of the rock bridges and lack of development of shear fabrics suggest that this model may be more appropriate than the model of Beach (1975) in this case. However, as with the model of Beach (1975), the rock bridge buckling mechanism cannot explain the greater rotation of the sigmoidal vein walls and fibres than older veinlets and minor veins. Fibres formed due to buckling of the rock bridges would also be expected to intersect vein walls at an oblique angle (Table 1), whereas most of the fibre-wall angles observed in the sample were close to 90° .

4.3 – Synthesis: Implications for slip partitioning, strain estimates and fluid communication.

In summary, the sigmoidal veins observed in the Cape Liptrap sample are not easily explained by existing models. Instead we propose that the pressure solution seams have played a crucial role in their development. The spatial association between pressure solution seams and sigmoidal en-

499 échelon veins was noted by Beach (1975), however the interaction between the two has never been
500 fully investigated.

501 Fletcher and Pollard (1981) have suggested that pressure solution seams can be treated as fractures
502 with negative displacements, or anticracks. They suggest that these structures often nucleate in the
503 zone of increased stress around the central portion of dilating veins, and then propagate outwards
504 to form a structure perpendicular to, and approximately the same length as, the vein.

505 Pressure solution seams forming in this way within an en-échelon vein array would quickly breach
506 the rock bridges separating the veins, dividing each rock bridge into lithons bounded by veins and
507 associated pressure solution seams. Consistent with the predictions of Fletcher and Pollard (1981)
508 the 3D structure mapping (Fig. 7) shows an association between the pressure solution seams and the
509 mid-points of many of the sigmoidal veins. In this example, it should also be noted that the pressure
510 solution seams are distributed along the full length of the longer veins, particularly on the left hand
511 side of the sample face (Fig. 7), and that some of the seams extend well beyond the boundaries of
512 the vein array.

513 We propose that slight rotation of these pressure solution seams during continued shear, causes
514 them to become oriented favourably for slip with respect to the far field stress. Similar development
515 of slip on pressure solution seams has been observed extensively in carbonate rocks (Peacock and
516 Sanderson, 1995; Tondi et al., 2006), and is thought to play a significant role during the nucleation of
517 faulting (Crider and Peacock, 2004; Graham et al., 2003; Willemse et al., 1997). Peacock and
518 Sanderson (1995) observed the development of pull-apart veins linked by sheared pressure solution
519 seams in the tips of brittle faults propagating through limestone. Likewise Fagereng et al., (2010)
520 describe pull-apart veins forming between sheared pressure solution seams within a sheared
521 mudstone.

522 A similar process could explain the dramatic changes observed in vein aperture where they are
523 crosscut by pressure solution seams (Fig. 11) and could explain the unusual geometry of the

sigmoidal veins in the Cape Liptrap sample. In our interpretation of the Cape Liptrap sample, slip on rotated pressure solution seams allows partitioning of strain during ongoing opening increments in the larger veins, leading to localised dilation within the central portion of the veins (Fig. 13). Offsets of the vein wall caused by this dilation explains the extreme rotations of sections of the vein wall observed in the sample, as well as the observed orientation of crystal fibres in the vein centres, while the older veinlets in the adjacent rock bridges are relatively less rotated.

Overall, early increments of strain in the Cape Liptrap sample have been expressed as widely distributed veinlets, presumably related to stochastic fracture nucleation within a tabular zone (Fig. 15a). Further deformation caused progressive strain localization (Fig. 15b) and the development of the pressure solution seams. As simple shear caused rotation of these structures, either through progressive rotation as suggest by Beach (1975), or through buckling (Nicholson and Pollard, 1985), the veins developed a subtle sigmoidal geometry and the pressure solution seams became oriented favourably for slip. Closely spaced veins also became linked by cross fractures (Fig. 15c). Finally, slip on pressure solution seams linking veins in the array caused localized dilation, exaggerating the geometry of the slightly sigmoidal veins during the later opening increments and changing the angular relationship between vein wall and fibres (Fig. 15d). Interestingly, in this later stage of growth vein lengths are essentially fixed and growth occurs mainly through slip-related dilation.

Our model of sigmoidal vein formation has implications for both strain estimates and fluid communication through the crust. Firstly, sigmoidal veins forming during slip partitioning on pressure solution seams develop vein-wall geometries that overestimate the degree of rotation. Thus it becomes critical that the role of pressure solution is properly assessed prior to quantification of simple shear and volume strain components of shear deformation (*c.f.* Lisle, 2013). Secondly, the veins have extreme in-plane lengths with channel-like geometries in 3D, and interlinking pressure solution seams. In addition, slip movement (and presumably transient permeability enhancement) has occurred on the linking pressure solution seams. These observations indicate that a high degree

of hydrological interconnectivity can be achieved through these vein networks (and interlinked pressure solution seams), over much larger distances than indicated by their cross-sectional geometry. In this example, those hydraulic distances exceed the depth of the sample (>15 cm for veins ~6 cm long), though the actual hydraulic transport distances are likely much greater.

5. Conclusions

The key findings of this study can be summarised as follows:

- Photogrammetry is a useful and accurate technique for collecting 3D structural data from hand samples. The model produced during this study was accurate to within 0.25mm and substantially more detailed than the reference laser scan.
- Veining and pressure solution initiated during early increments of strain and became critical components of the resulting shear deformation and fracture mechanics. After the early veins formed, strain progressively localised onto fewer but larger structures.
- Pressure solution seams and early formation of veinlets provided markers to assess the deformation that occurred during the development of a sigmoidal vein array. Rotation of these markers was not great enough to fully explain the geometry of the sigmoidal veins. Instead, slip appears to partition onto pressure solution seams that have undergone small rotations, causing localized dilation and the exaggeration of sigmoidal vein geometries.
- CT models demonstrate that the veins have channel-like geometries in 3D, penetrating the entire sample, which indicates that the veins had much greater capacity for linkage and the communication of crustal fluids than their 2D form suggests.
- Volume strain and simple shear calculations from sigmoidal veins will overestimate angular strain for vein arrays of this type, when pressure solution is also operative, because the partitioning of both pure and simple shear onto pressure solution seams allows the veins to become highly sigmoidal without requiring substantial rotation or buckling. Thus an

assessment of the role of pressure solution should be made before applying any techniques that estimate strain from vein geometry.

Acknowledgements

This study derives from an honours thesis by S. Thiele. S. Micklethwaite acknowledges support from the Hammond-Nisbet Fellowship. The authors would also like to thank Ake Fagereng and Betsy Madden for their detailed and constructive reviews.

6. References Cited

- Allmendinger, R.W., Cardozo, N., Fisher, D.M., 2011. Structural Geology Algorithms: Vectors and Tensors. Cambridge University Press.
- Beach, A., 1975. The geometry of en-echelon vein arrays. *Tectonophysics* 28, 245-263.
- Belayneh, M., Cosgrove, J.W., 2010. Hybrid veins from the southern margin of the Bristol Channel Basin, UK. *Journal of Structural Geology* 32, 192-201.
- Bemis, S.P., Micklethwaite, S., James, M.R., Turner, D., Akciz, S., Thiele, S., Bangash, H.A., 2014. Ground-based and UAV-based photogrammetry: A multi-scale, high-resolution mapping tool for structural geology and paleoseismology. *Journal of Structural Geology*.
- Cignoni, P., Corsini, M., Ranzuglia, G., 2008. Meshlab: an open-source 3d mesh processing system. *Ercim news* 73, 45-46.
- Cignoni, P., Rocchini, C., Scopigno, R., 1998. Metro: Measuring error on simplified surfaces, *Computer Graphics Forum*. Wiley Online Library, pp. 167-174.
- Crider, J.G., Peacock, D.C.P., 2004. Initiation of brittle faults in the upper crust: a review of field observations. *Journal of Structural Geology* 26, 691-707.
- Davis, G.H., Reynolds, S.J., Kluth, C., 1996. Structural geology of rocks and regions.
- Douglas, J.G., 1972. Explanatory notes on the Liptrap 1:63 360 geological map, in: Victoria, G.S.O. (Ed.).

597 Fabio, R., 2003. From point cloud to surface: the modeling and visualization problem. International
 598 Archives of Photogrammetry, Remote Sensing and Spatial Information Sciences 34, W10.

599 Fagereng, Å., Remitti, F., Sibson, R.H., 2010. Shear veins observed within anisotropic fabric at high
 600 angles to the maximum compressive stress. Nature Geoscience 3, 482-485.

601 Favalli, M., Fornaciai, A., Isola, I., Tarquini, S., Nannipieri, L., 2012. Multiview 3D reconstruction in
 602 geosciences. Computers & Geosciences 44, 168-176.

603 Fischler, M.A., Bolles, R.C., 1981. Random sample consensus: a paradigm for model fitting with
 604 applications to image analysis and automated cartography. Commun. ACM 24, 381-395.

605 Fletcher, R.C., Pollard, D.D., 1981. Anticrack model for pressure solution surfaces. Geology 9, 419-
 606 424.

607 Fossen, H., 2010. Structural Geology. Cambridge University Press, Cambridge.

608 Graham, B., Antonellini, M., Aydin, A., 2003. Formation and growth of normal faults in carbonates
 609 within a compressive environment. Geology 31, 11-14.

610 Gray, D.R., Janssen, C., Vapnik, Y., 1999. Deformation character and palaeo-fluid flow across a
 611 wrench fault within a Palaeozoic subduction–accretion system: Waratah Fault Zone,
 612 southeastern Australia. Journal of Structural Geology 21, 191-214.

613 Grohmann, C., Campanha, G., 2010. OpenStereo: open source, cross-platform software for structural
 614 geology analysis, AGU Fall Meeting abstracts, p. 06.

615 James, M., Robson, S., 2014. Systematic vertical error in UAV-derived topographic models: origins
 616 and solutions.

617 Janssen, C., Laube, N., Bau, M., Gray, D.R., 1998. Fluid regime in faulting deformation of the Waratah
 618 Fault Zone, Australia, as inferred from major and minor element analyses and stable isotopic
 619 signatures. Tectonophysics 294, 109-130.

620 Lennox, P.G., Golding, S.D., 1989. Quartz veining in simply folded arenites, Cape Liptrap, southeast
 621 Victoria, Australia. Australian Journal of Earth Sciences 36, 243-261.

622 Limaye, A., 2012. Drishti: a volume exploration and presentation tool, pp. 85060X-85060X-85069.

623 Lisle, R.J., 2013. Shear zone deformation determined from sigmoidal tension gashes. *Journal of*
 624 *Structural Geology* 50, 35-43.

625 Lowe, D.G., 2004. Distinctive image features from scale-invariant keypoints. *International journal of*
 626 *computer vision* 60, 91-110.

627 Micklethwaite, S., Sheldon, H.A., Baker, T., 2010. Active fault and shear processes and their
 628 implications for mineral deposit formation and discovery. *Journal of Structural Geology* 32, 151-
 629 165.

630 Nicholson, R., Pollard, D.D., 1985. Dilation and linkage of echelon cracks. *Journal of Structural*
 631 *Geology* 7, 583-590.

632 Olson, J.E., Pollard, D.D., 1991. The initiation and growth of en échelon veins. *Journal of structural*
 633 *geology* 13, 595-608.

634 Peacock, D.C.P., Sanderson, D.J., 1995. Pull-aparts, shear fractures and pressure solution.
 635 *Tectonophysics* 241, 1-13.

636 Piper, J., 2010. Software-Based Stacking Techniques to Enhance Depth of Field and Dynamic Range in
 637 Digital Photomicrography, in: Hewitson, T.D., Darby, I.A. (Eds.), *Histology Protocols*. Humana
 638 Press, pp. 193-210.

639 Pollard, D.D., Segall, P., Delaney, P.T., 1982. Formation and interpretation of dilatant echelon cracks.

640 Pollefeys, M., Koch, R., Van Gool, L., 1999. Self-calibration and metric reconstruction inspite of
 641 varying and unknown intrinsic camera parameters. *International Journal of Computer Vision* 32,
 642 7-25.

643 Rickard, M.J., Rixon, L.K., 1983. Stress configurations in conjugate quartz-vein arrays. *Journal of*
 644 *Structural Geology* 5, 573-578.

645 Riedel, W., 1929. Zur mechanik geologischer brucherscheinungen. *Zentralblatt für Mineralogie,*
 646 *Geologie und Paläontologie B* 1929, 354-368.

647 Shainin, V.E., 1950. Conjugate sets of en echelon tension fractures in the Athens Limestone at
 648 Riverton, Virginia. *Geological Society of America Bulletin* 61, 509-517.

649 Slizewski, A., Semal, P., 2009. Experiences with low and high cost 3D surface scanner. *Quartär* 56,
650 131-138.

651 Sturm, P., Triggs, B., 1996. A factorization based algorithm for multi-image projective structure and
652 motion, *Computer Vision—ECCV'96*. Springer, pp. 709-720.

653 Tanner, P.W.G., 1992. Vein morphology, host rock deformation and the origin of the fabrics of
654 echelon mineral veins: Discussion. *Journal of Structural Geology* 14, 373-375.

655 Tondi, E., Antonellini, M., Aydin, A., Marchegiani, L., Cello, G., 2006. The role of deformation bands,
656 stylolites and sheared stylolites in fault development in carbonate grainstones of Majella
657 Mountain, Italy. *Journal of Structural Geology* 28, 376-391.

658 Triggs, B., McLauchlan, P.F., Hartley, R.I., Fitzgibbon, A.W., 2000. Bundle adjustment—a modern
659 synthesis, *Vision algorithms: theory and practice*. Springer, pp. 298-372.

660 Twiss, R., Moores, E., 2007. *Structural Geology*. WH Freeman and Company, New York.

661 Willemse, E.J.M., Peacock, D.C.P., Aydin, A., 1997. Nucleation and growth of strike-slip faults in
662 limestones from Somerset, U.K. *Journal of Structural Geology* 19, 1461-1477.

663 Willmott, C.J., Matsuura, K., 2005. Advantages of the mean absolute error (MAE) over the root mean
664 square error (RMSE) in assessing average model performance. *Climate Research* 30, 79.

665

666

Figure Captions

Fig. 1. Schematic geology map of the Cape Liptrap region (a), including the location from where the study sample (b) was collected. Modified from Janssen et al. (1998).

Fig. 2. Models of sigmoidal vein formation. (a) The kinematic model of Beach (1975) with veins, originally parallel to the maximum principal stress axis, rotating under simple shear within a shear zone. The sigmoidal shape forms as vein tips continue to propagate parallel to the principal stress axis. (b) Mechanical model of Nicholson and Pollard (1985), showing progressive buckling of rock bridges between veins, which then induces a component of shear to the rock mass. (c) Mechanical model of Olson and Pollard (1991), showing sigmoidal geometry formed by fracture-tip interactions between fractures in a growing en-échelon array.

Fig. 3. Schematic diagram illustrating the process used to extract planes from the 3D structural maps. The intersection of each structural feature and the specimen surface is represented by a series of linked vertices (a). Note that the roughness of this line has been exaggerated for illustrative purposes. A subset of specified size ($n=14$) is taken from this dataset (b) and its principal components (C_1 , C_2 and C_3) calculated. The principal components are used to evaluate planarity (p , Eq. 1). When $P > 0.75$, a plane is fitted to the data using the RANSAC algorithm (Fischler and Bolles, 1981). Individual trials (c), (d) and (e) select three random points and calculate the number of points falling within a threshold distance of the plane they define (inliers). The required sample size (N) to be 99% sure the correct plane has been trialled at least once is calculated based on the probability (p) of choosing three inliers. Once the number of trials is equal to the smallest N , the plane with the greatest number of inliers (d) is used to calculate a final plane, by least squares regression after removing outliers (f).

Fig. 4. Accuracy and quality of the photogrammetric models. Error maps show the differences between the photogrammetric and laser scan models. A render of the laser scan is included as Fig.

5a. Normal maps created by mapping the x, y and z values of each faces normal to red, green and blue colour values show the detail of the underlying mesh, while the texture maps show the quality of the textures. Note that the close-up of the texture has been rotated. Model A is clearly the most accurate, with lower MAE values than all the other models and a 'crisper' normal map. The texture quality of Model A is also superior to the other models, without obvious pixilation or distortion.

Fig. 5. Maps of the laser scan model (a) and photogrammetric Model A (b) created by mapping the x, y and z component of each mesh elements normal to the red, green and blue channels of the face colour. Subtle features such as calcite fibres within the veins and the thickness of the reference marker are clearly visible in the photogrammetric model, whereas the laser scan model contains significantly less detail. Many of the differences between the laser scan and photogrammetric model (c) could simply result from this difference in resolution, suggesting that the photogrammetric model is more accurate than the laser scan.

Fig. 6. Renders of the front (a) and back (b) of Model A, generated from a set of 516 images with the final mesh decimated to 1 million faces. This model has the highest accuracies, and was the model selected for interpretation. The vein array of interest and the associated pressure solution seams are clearly resolvable. The model was scaled and distortions minimised through the use of orange markers, where the distances between each marker were accurately constrained using electronic calipers.

Fig. 7. Structure maps created using the front (a) and back (b) of photogrammetric Model A. Veins are divided into three sets: major (light green), minor (dull green) and veinlets (dark green). Pressure solution seams are shown in red and vein fibres in grey. 3D structure orientations extracted from these maps are shown in (c) and (d). Pole orientations have been contoured using the Kamb Method at intervals of 2σ and a significance of 3σ . Note that poles plotting towards the centre of each stereonet are likely artefacts introduced by the plane-fitting algorithm, and do not represent the true orientation of veins.

Fig. 8. Mean intersection angles between structures and the interpreted shear envelope. (a) The intersection angles of each major (sigmoidal) vein wall (bright green dots), minor vein (dull green dots), veinlet (blue dots) and pressure solution seam (PSS, red dots) were measured in each portion of the shear envelope. Note that for clarity only the three well-developed sigmoidal veins have been included. (b) Boxplots show that the intersection angle the structures tend to increase towards the centre of the envelope, however not by the same amount. The orientation of the sigmoidal vein walls increases by an average of 27° towards the centre of the shear envelope, whereas the orientations of the veinlets, minor veins and PSS only increase by 7°, 11° and 12° respectively (Table 3).

Fig. 9. Spatial variation in vein fibre orientation. Vein fibres are coloured by deviations from their average orientation in vein tips. The crystal fibres in the central sections of the sigmoidal deviate by 30-40° to this value. Dots along vein margins show the angle between the vein fibres and vein walls as deviations from 90°. Most fibre wall angles approximate 90°, although there are exceptions.

Fig. 10. Photomicrographs showing crosscutting relationships within the sample. Veinlets are crosscut by larger veins in insets (a), (b), (e), (f), (g) and (j). Inset (h) shows a veinlet that appears to crosscut one of the sigmoidal veins. The minor veins are also shown to be crosscut by the sigmoidal veins in (c), (d) and (j).

Fig. 11. Interactions between veins and pressure solution seams. The pressure solution seams in all plates clearly divide zones that have undergone different amounts of strain, or have strained in different ways. Veins in (a), (b) and (c) show offset across pressure solution seams. Step changes in vein aperture (red highlights) coincide with intersections between pressure solution seams displaying offset and vein margins.

Fig. 12. Drishti renderings of the CT dataset. (a) Plan view slices of the vein array. (b) Cross-sections of the vein array. (c) Longitudinal sections of the vein array. The plan sections (a) are perpendicular

to the orientation of the vein array and long sections (c) are parallel to it. Veins and pressure solution seams (PSS) interpreted from these data are shown in (d).

Fig. 13. Interactions between pressure solution seams (dashed red lines) and sigmoidal veins observed in the photogrammetric micrograph. Unusually oriented sections of the vein walls correlate with offset on the pressure solution seams and increases in vein aperture.

Fig. 14. Sequence diagram showing the interpreted order of formation of the veinlets, minor veins, major veins and pressure solution seams (PSS) observed within the sample (see Fig. 10 and section 3.4).

Fig. 15. Conceptual model for the development of a vein array similar to the one observed in the Cape Liptrap sample. (a) Veinlets develop from a broad zone of microfractures during early increments of shear. Possible early pressure solution. (b) Competition between veinlets and progressive linkage causes strain localization onto fewer, larger veins. Pressure solution seams initiate and propagate as anticracks, generally originating from the centre of veins (Fletcher and Pollard, 1981). (c) Subtle sigmoidal geometry develops as veins rotate within the shear zone, either due to the mechanism of Beach (1975) or Nicholson and Pollard (1985). Rotated pressure solution seams become oriented favourably for slip and begin to partition both pure and simple shear strain. Rock bridges separating closely spaced veins are breached by cross fractures as vein dilation increases. (d) Slip on pressure solution seams enhances dilation within vein centres, amplifying their sigmoidal geometry.

762 **Table Captions**

763 **Table 1:** Model predictions for vein formation regarding vein geometry, deformation within rock
764 bridges separating veins and orientation of vein fibres. Note that while the specific orientation of
765 vein fibres will depend on the opening mechanisms of the veins, in the criteria listed the first-order
766 orientation/misorientation is assumed to be tracking vein opening and deformation.

767 **Table 2:** Mean structure orientations based on planes extracted from the structure maps using
768 RANSAC. The 95% confidence interval around each mean is also shown, as is the sample size (n). A
769 95% confidence interval was not calculated for minor veins as the sample size (14) is not large
770 enough to produce a meaningful result.

771 **Table 3:** Mean intersection angles between structures and portions of the shear envelope (Fig. 8).
772 Structures outside or within the outer portion of the shear envelope (outer) are considered to
773 represent the initial orientation of structures within the centre of the shear envelope (inner). Hence,
774 the difference between the mean inner intersection angle and mean outer intersection angle gives
775 the apparent rotation that the structure has undergone within the shear zone. The

fig 1

[Click here to download high resolution image](#)

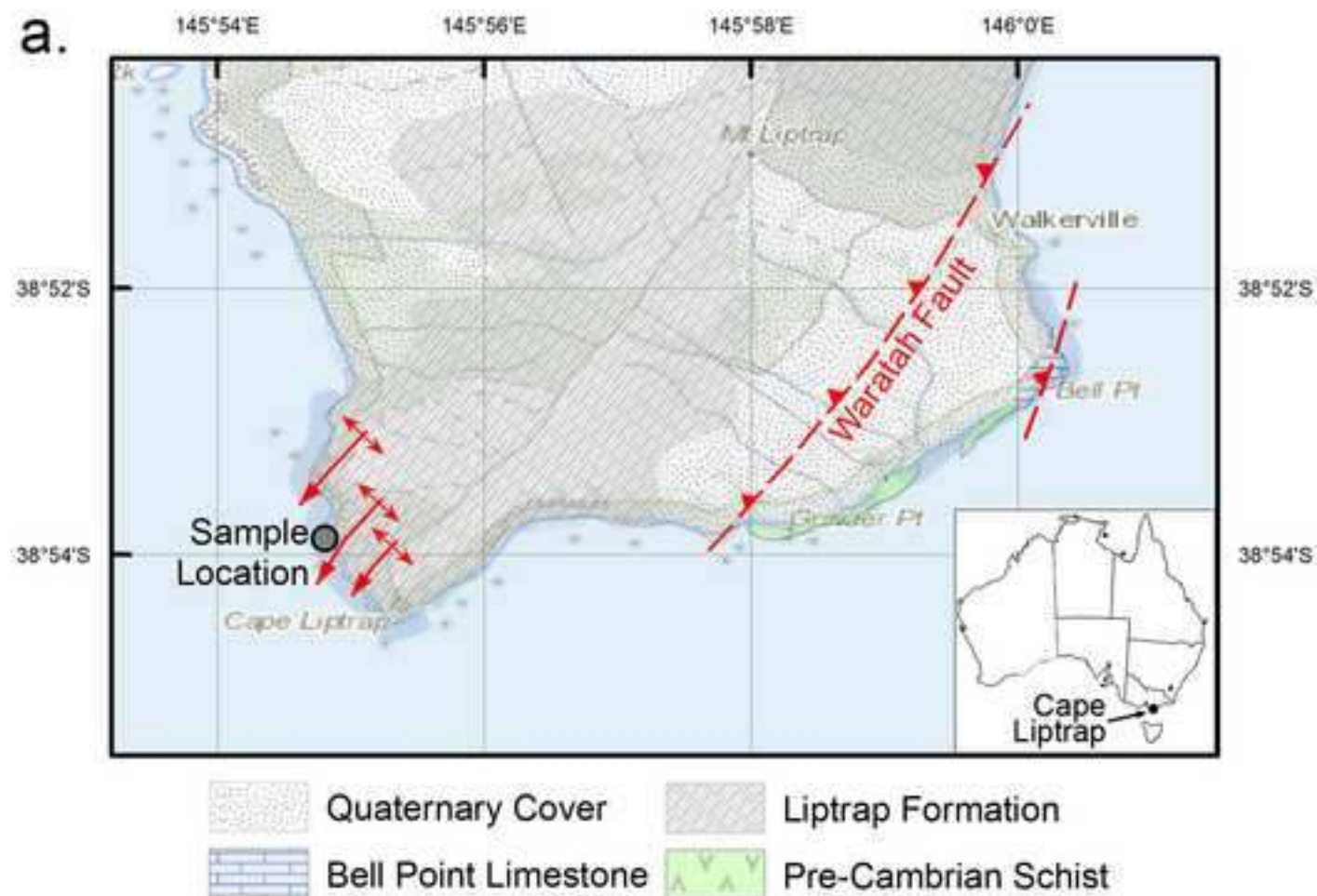
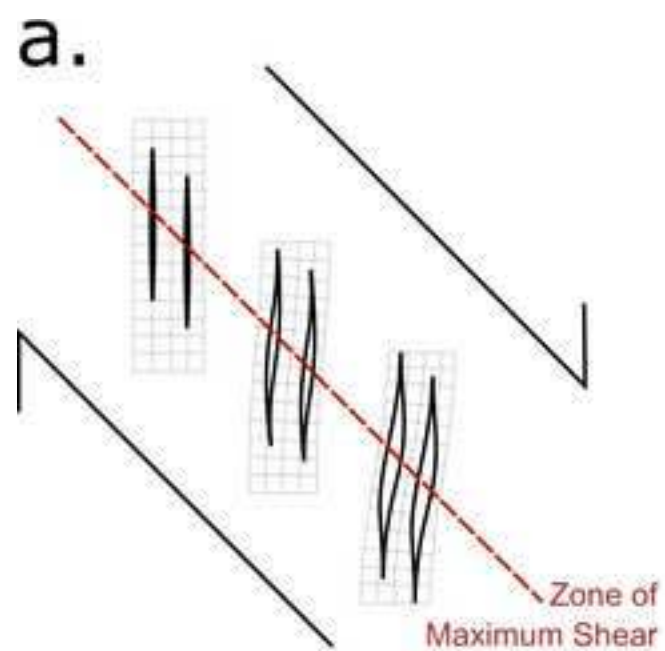
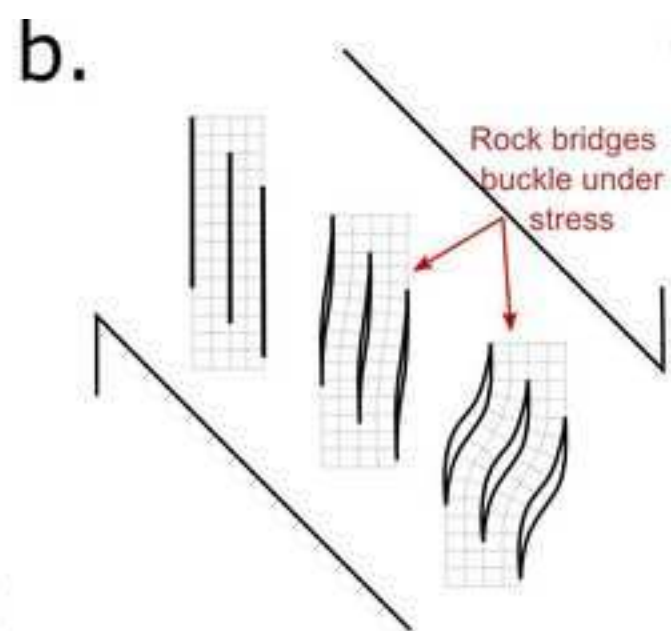


fig 2

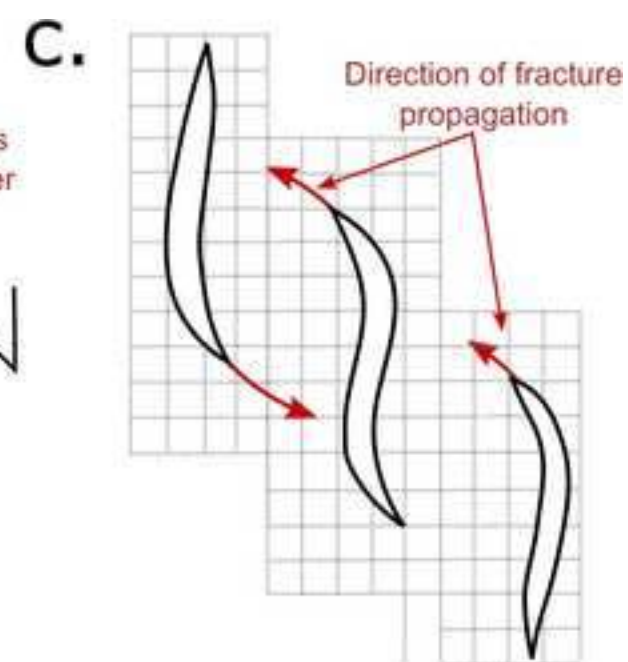
[Click here to download high resolution image](#)



Beach (1975)



Nicholson & Pollard
(1985)

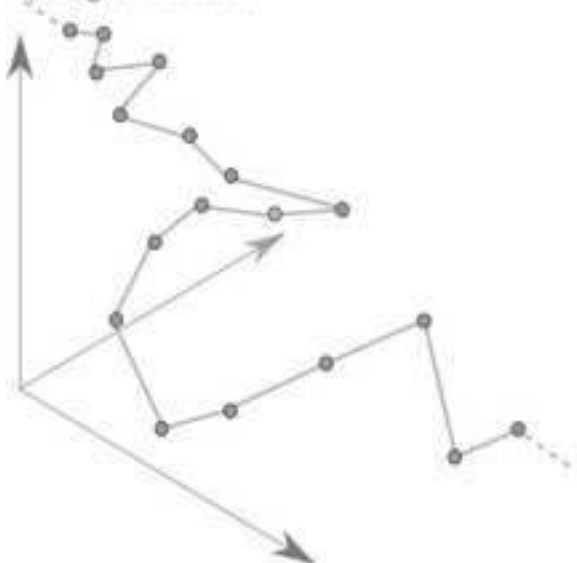


Olson, Olson &
Pollard (1991)

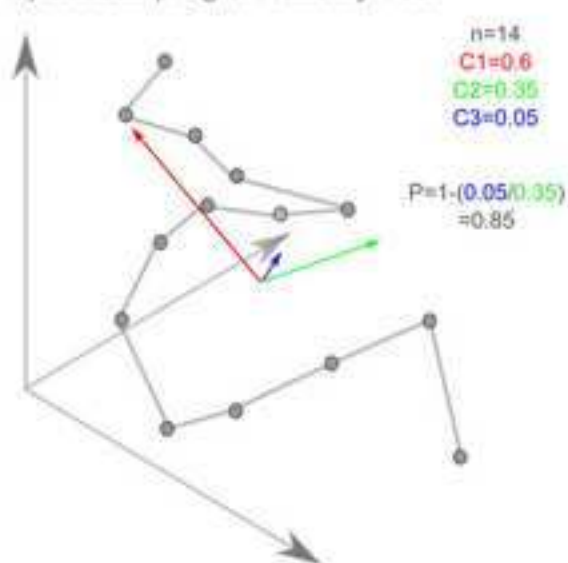
fig 3

[Click here to download high resolution image](#)

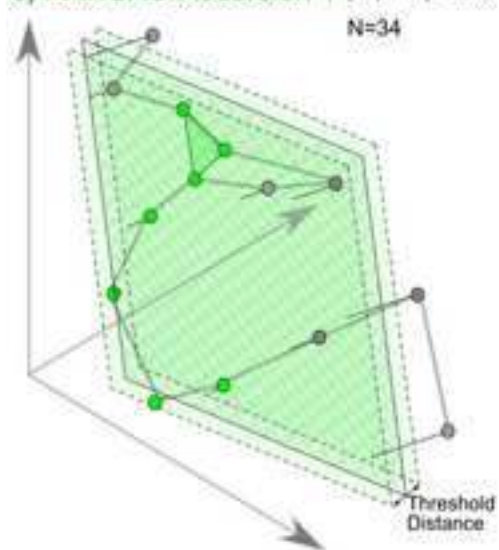
a) Original Dataset



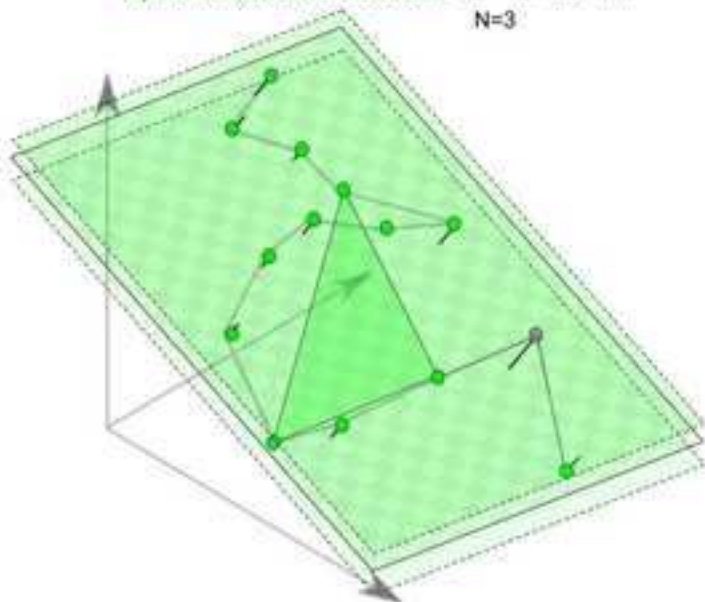
b) Subsampling & Planarity Test



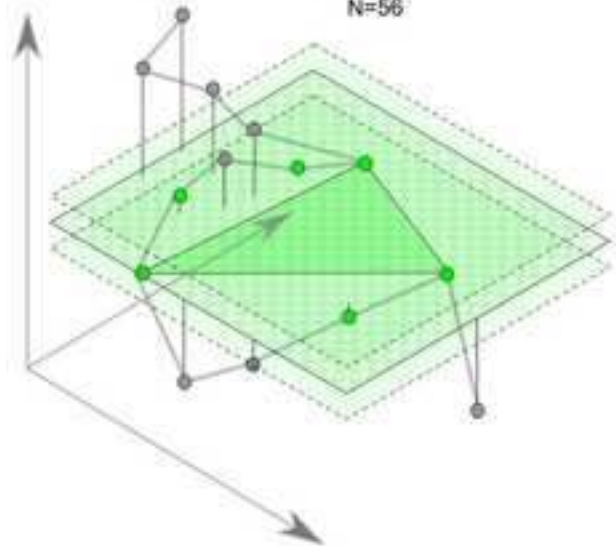
c) RANSAC Recursion 1 $p=(7/14)^3=0.13$
N=34



d) RANSAC Recursion 2 $p=(13/14)^3 \approx 0.8$
N=3



e) RANSAC Recursion 3 $p=(6/14)^3=0.08$
N=56



f) Least Squares Regression

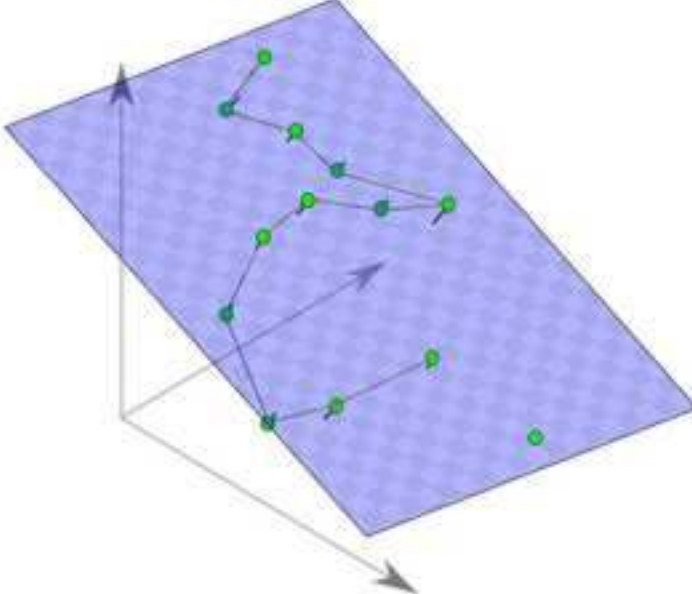


fig 4

[Click here to download high resolution image](#)

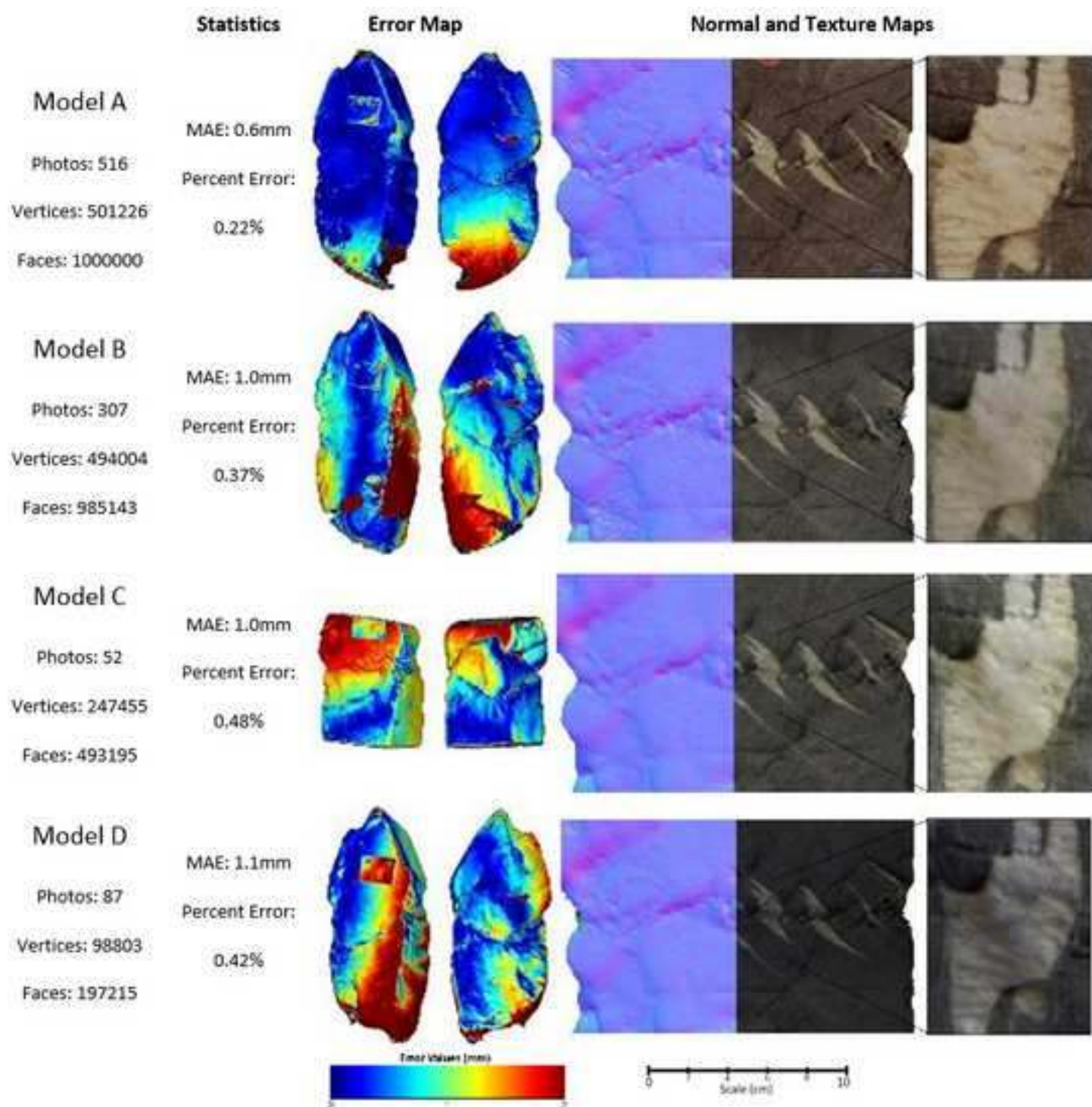


fig 5

[Click here to download high resolution image](#)

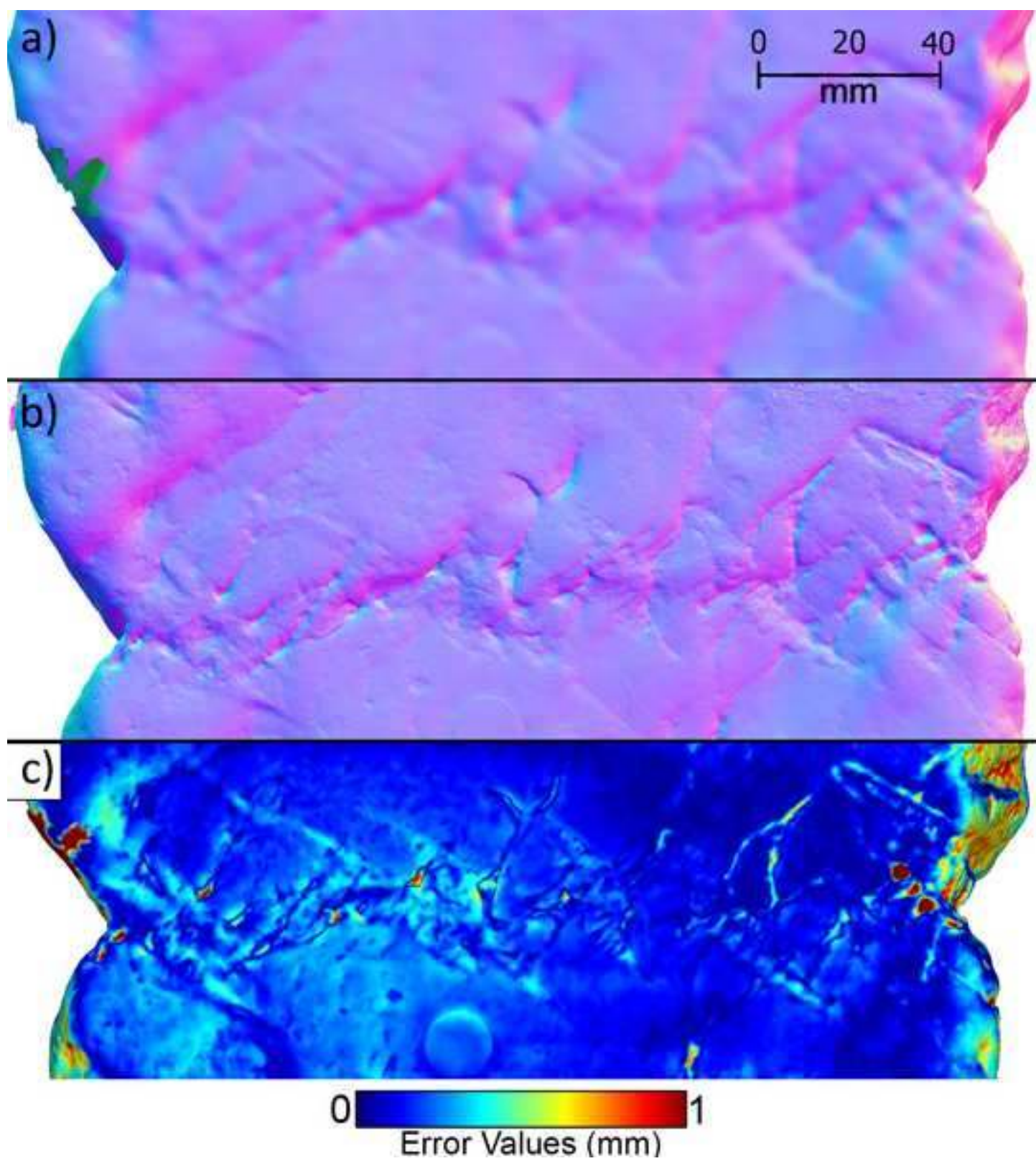


fig 6

[Click here to download high resolution image](#)

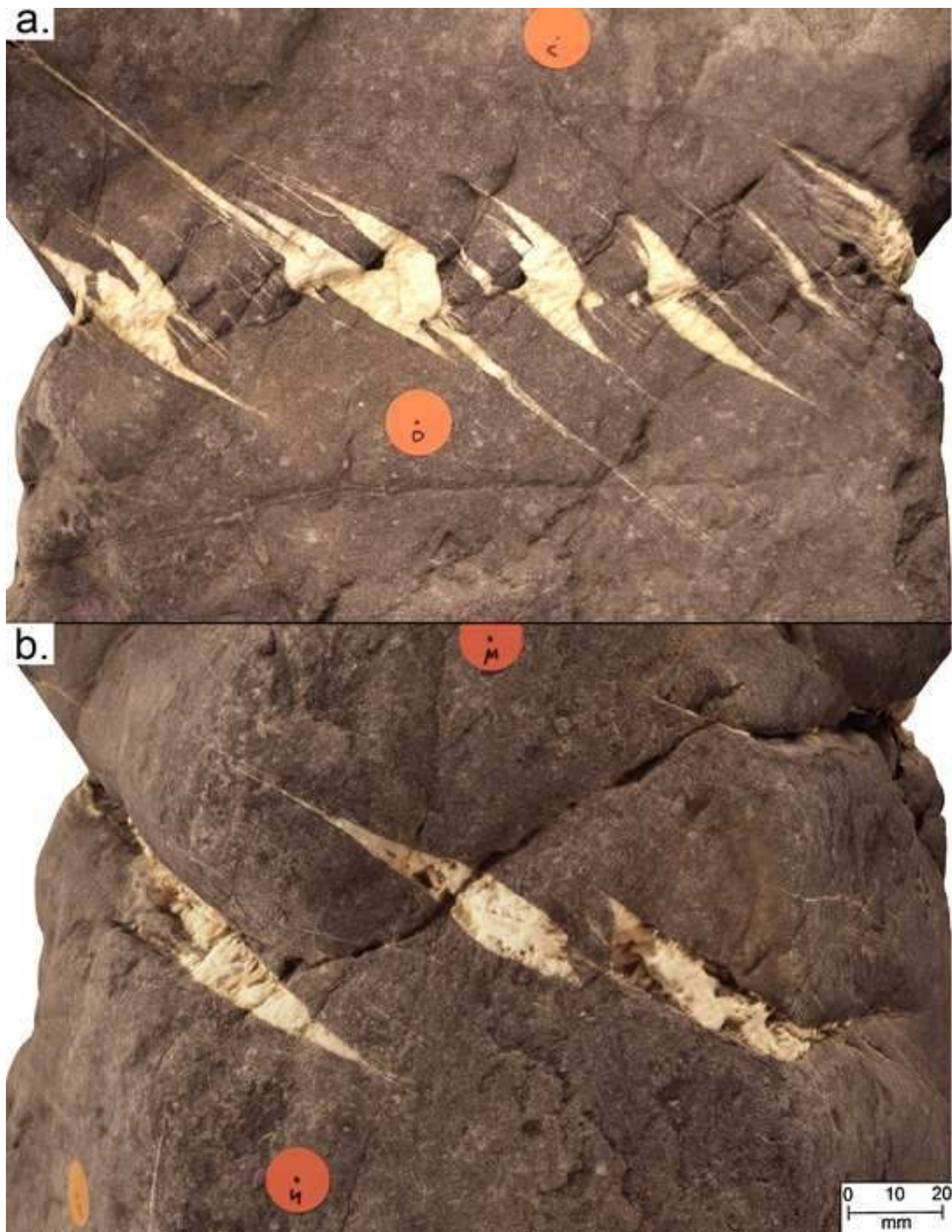


fig 7

[Click here to download high resolution image](#)

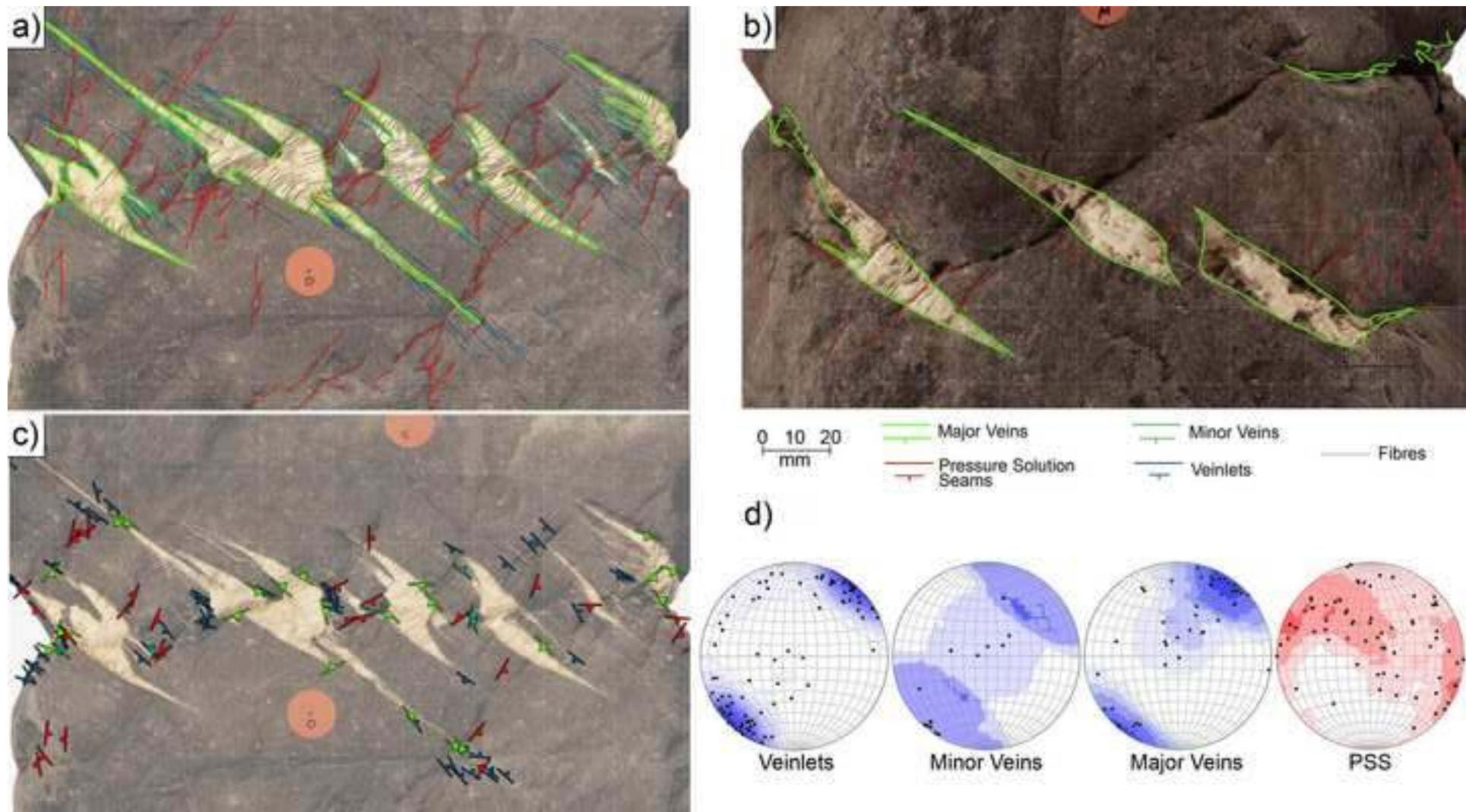


fig 8

[Click here to download high resolution image](#)

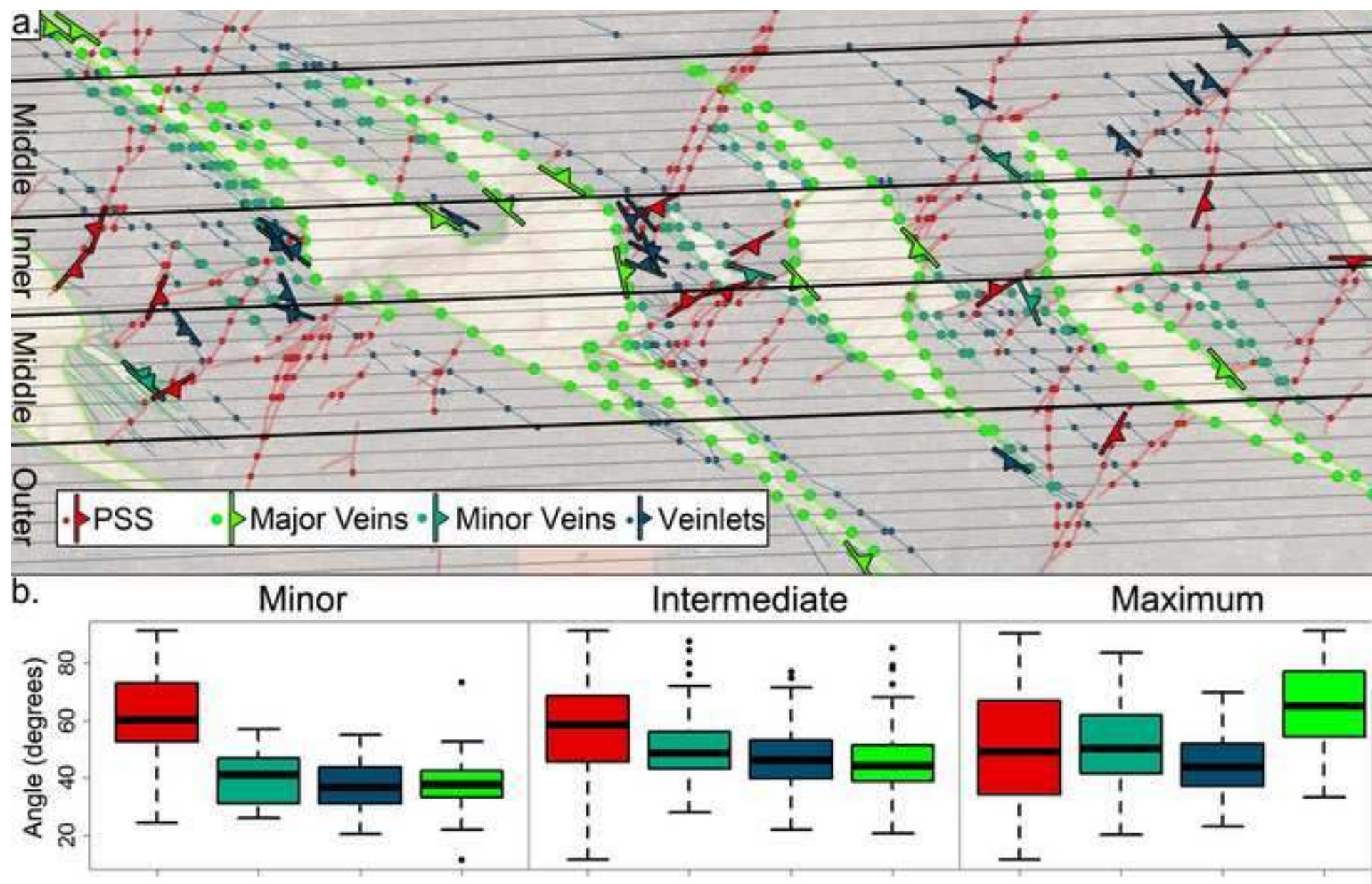


fig 9

[Click here to download high resolution image](#)

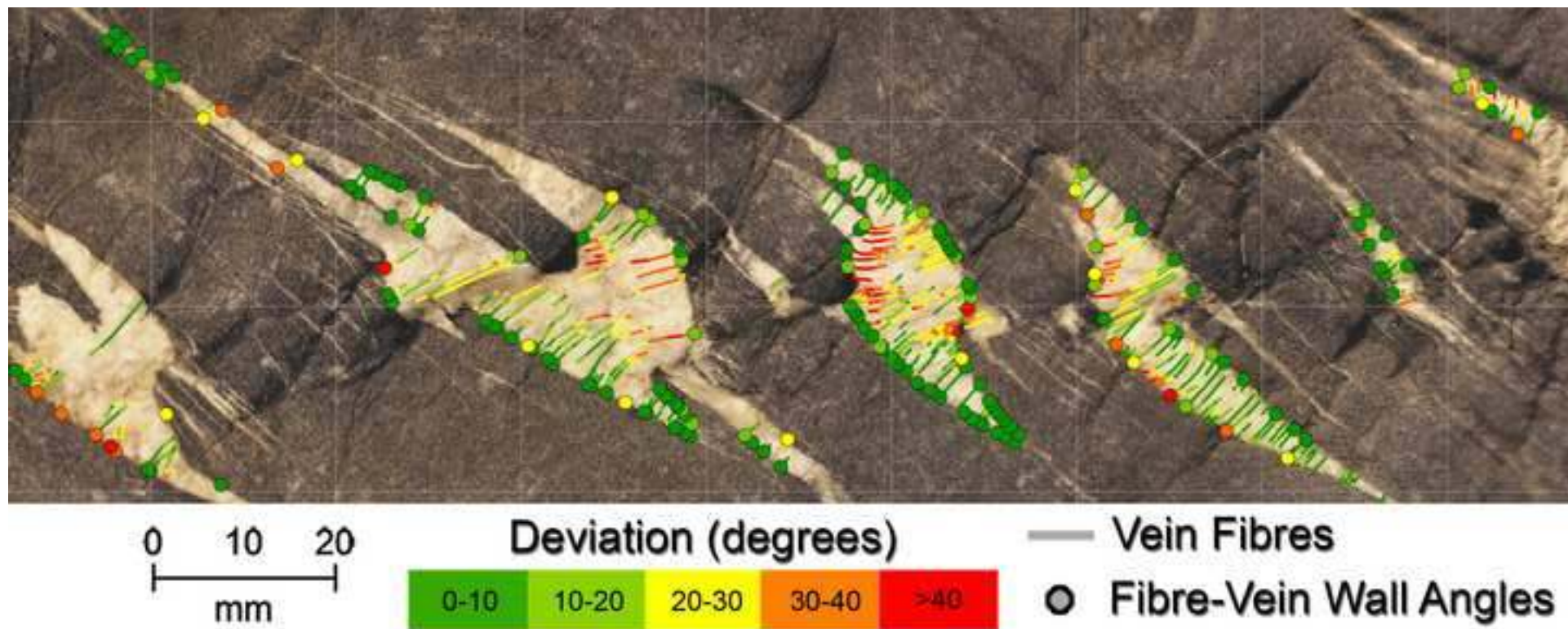


fig 10

[Click here to download high resolution image](#)



fig 11

[Click here to download high resolution image](#)

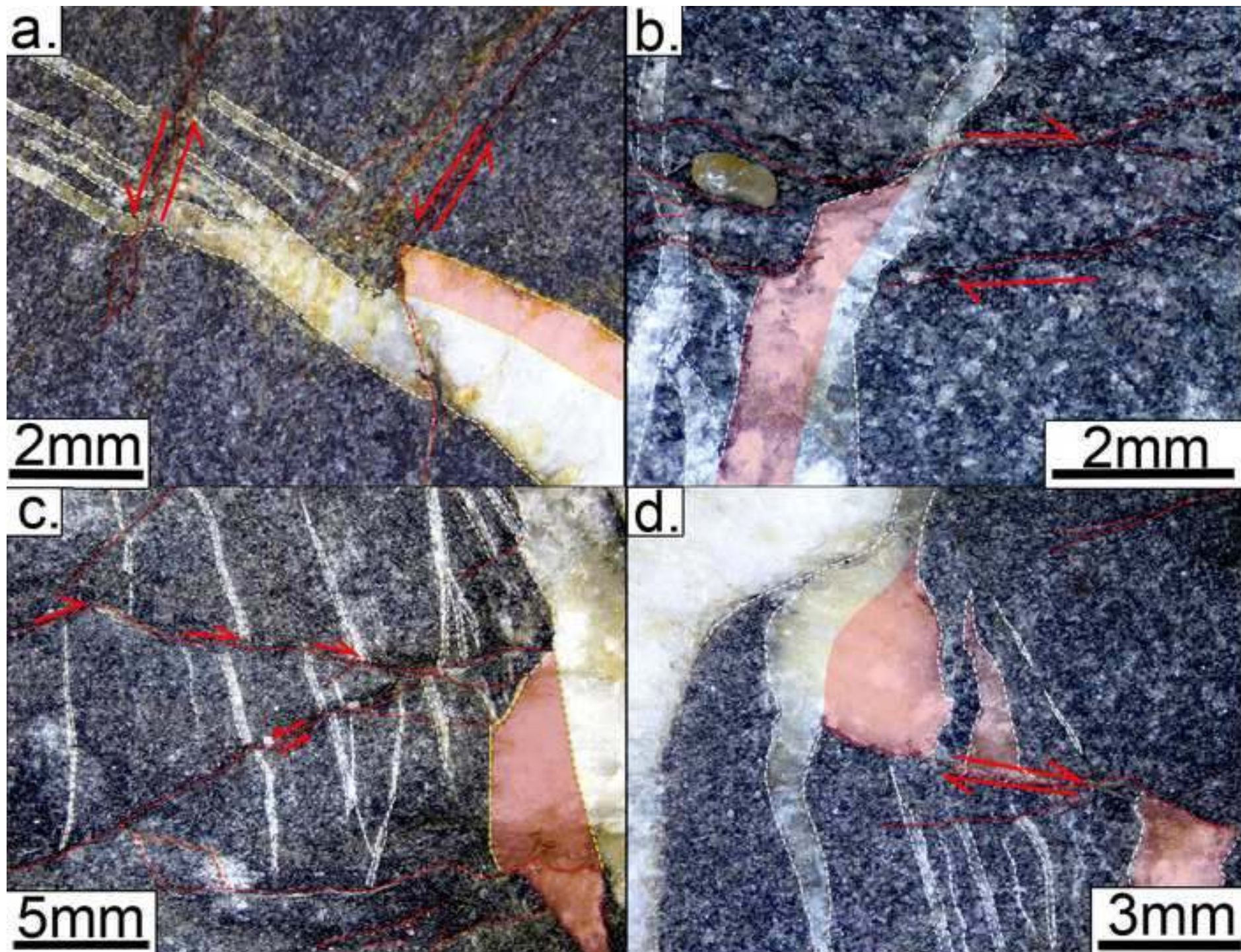


fig 12

[Click here to download high resolution image](#)

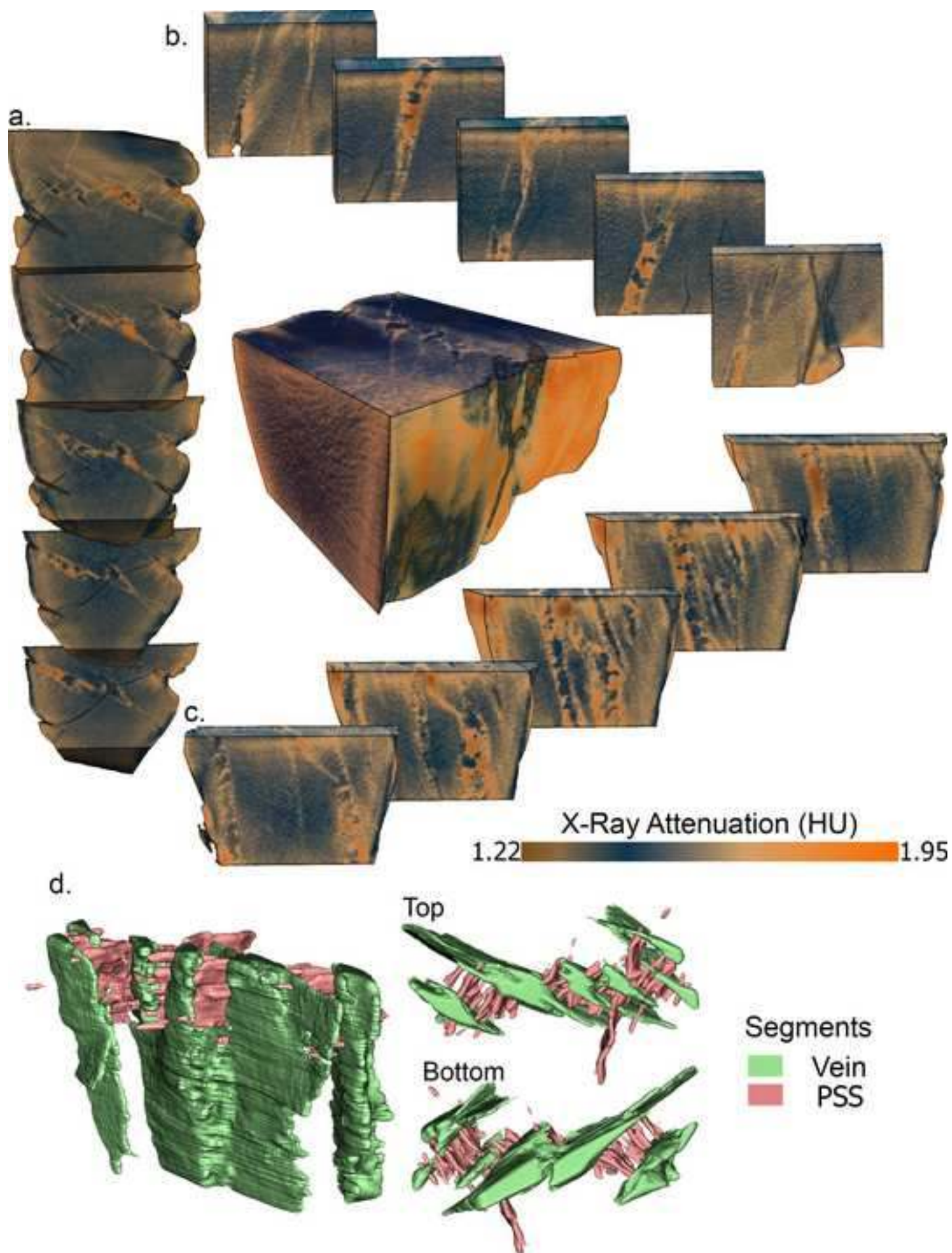


fig 13

[Click here to download high resolution image](#)

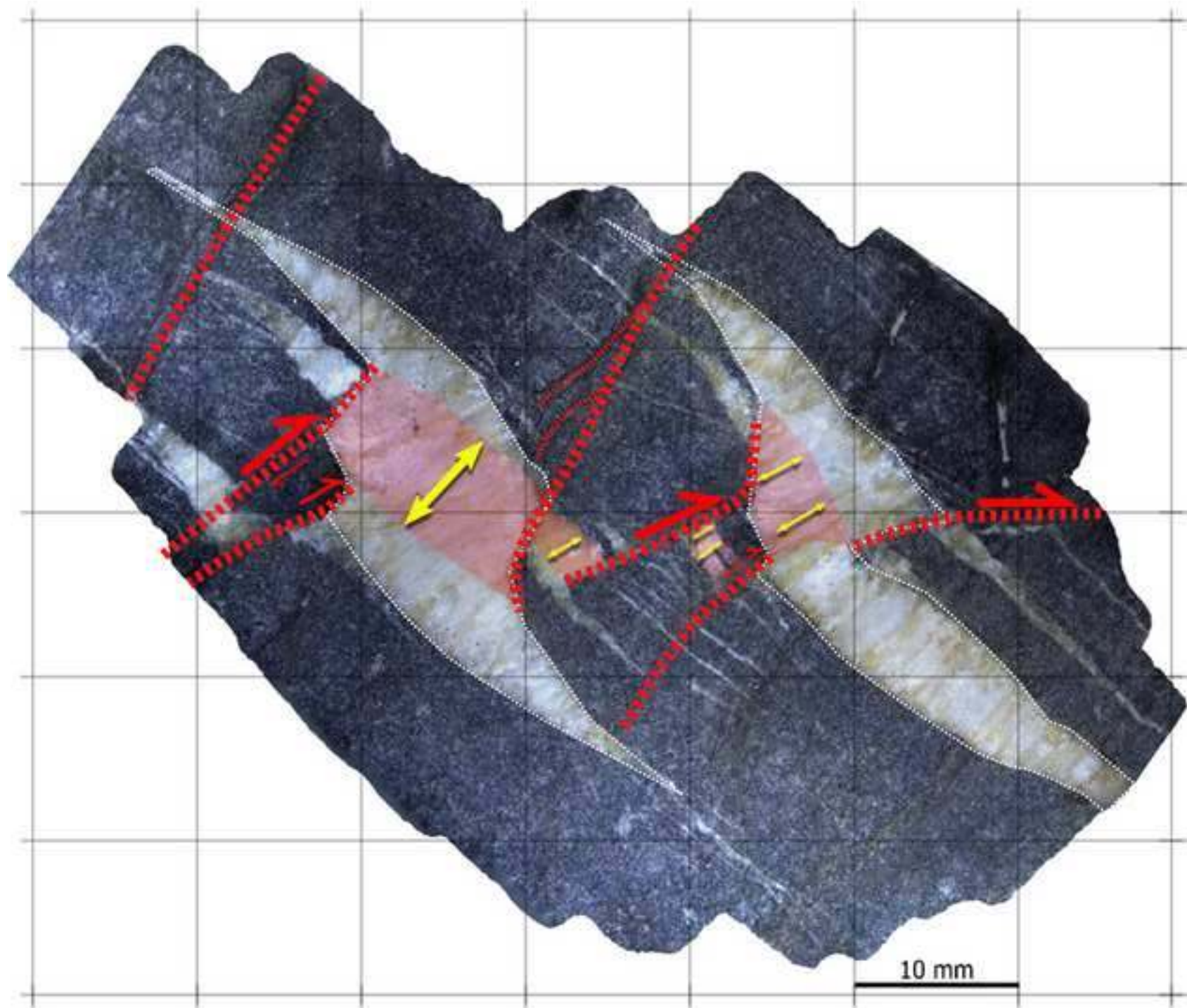


fig 14

[Click here to download high resolution image](#)

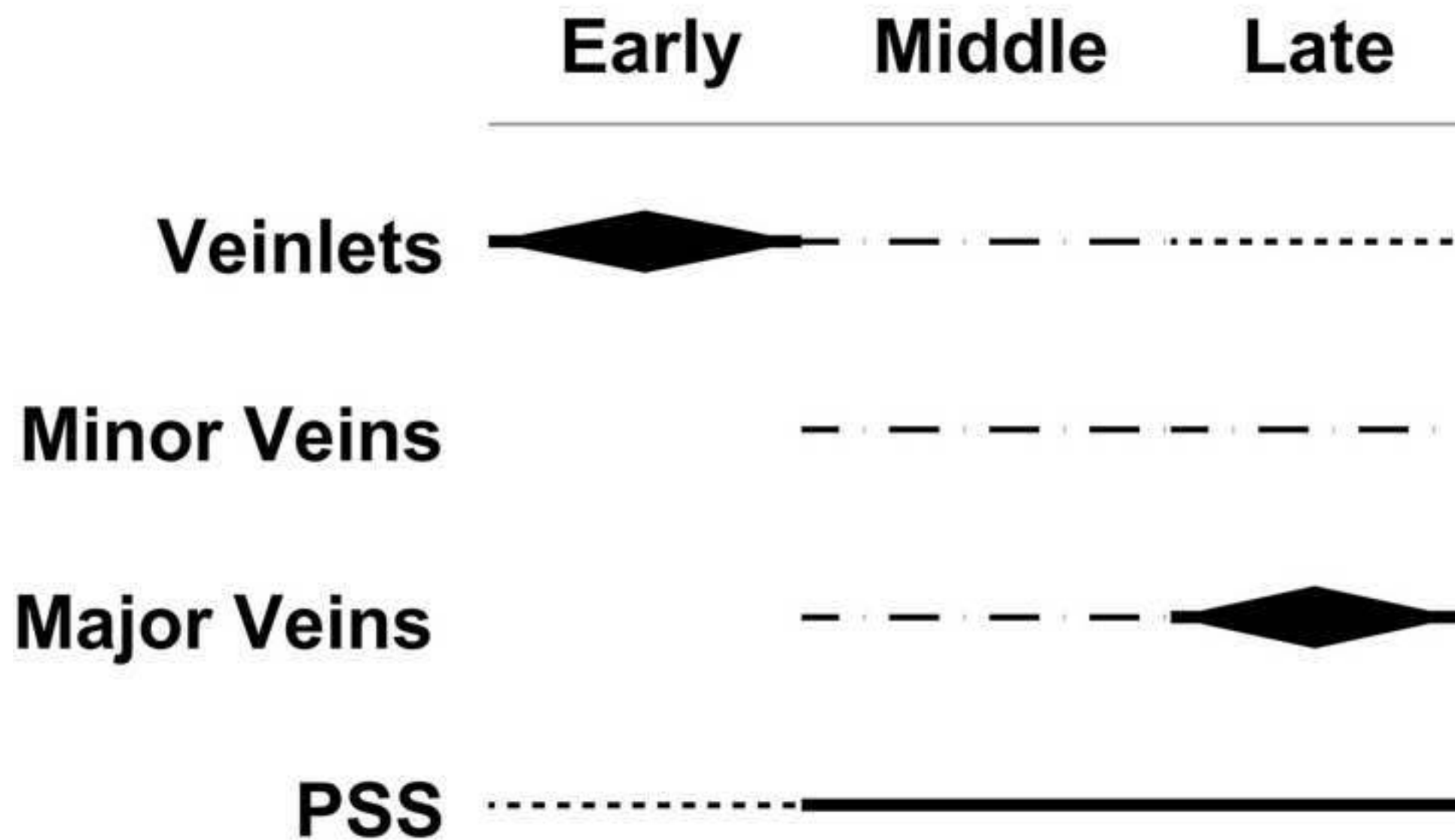


fig 15

[Click here to download high resolution image](#)

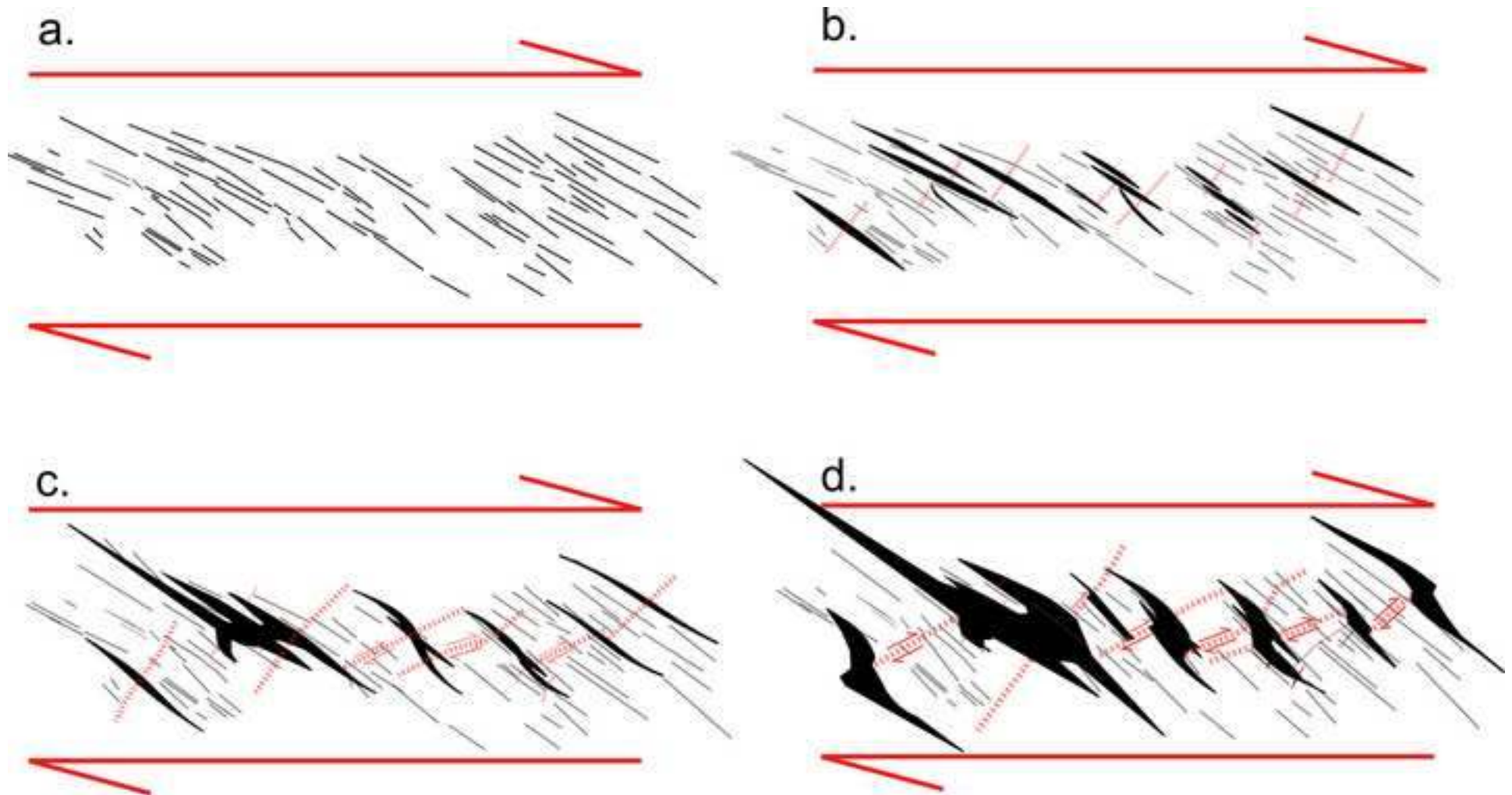


Table1

Model	Vein Geometry	Deformation of Rock Bridges	Vein Fibres
Beach (1975)	Central portions of veins misoriented with respect to far field stress.	Rock bridges deformed by shearing; older structures and fabrics in rock bridges are rotated by the same amount or more than vein walls.	Vein fibres rotated with veins; vein fibres oriented perpendicular to vein walls.
Nicholson and Pollard (1985)	Overlapping portions of vein walls misoriented with respect to far field stress.	Rock bridges buckled due to vein dilation; older structures and fabrics in rock bridges are rotated by the same amount as vein walls.	Vein fibres oriented obliquely to vein wall across misoriented sections.
Olson et al. (1991)	Tips of veins misoriented with respect to far field stress.	No rotation of older structures in rock bridges; vein tips will crosscut older structures and fabrics.	Vein fibres oriented perpendicular to vein walls.

Table 2

Statistic	Veinlets	Minor Veins	Major Veins	Pressure Solution Seams
Mean Orientation	310.1°/87.3°E	129.3°/57°W	123.5°/75.1°W	033.1°/66.7°E
95% Confidence Interval	±6.2°	-	±15.9°	±61.7°
N	91	14	43	70

Table 3

Structure	Mean Intersection Angle			Apparent Rotation
	Outer	Middle	Inner	
Veinlets	37°	42°	44°	7°
Minor Veins	40°	46°	51°	11°
Pressure Solution Seams	62°	54°	50°	12°
Sigmoidal Veins	37°	41°	64°	27°